

Nitrogen doped thin films of cuprous oxide

Ida Marie Bentsen

August 2017

Contents

1	Abstract	3
2	Motivation: Why p+ Cu₂O?	4
3	Theory	5
3.1	Energy bands	5
3.2	Semiconductors	5
3.3	Crystal structure	5
3.4	Defects and doping	6
3.5	Solar cells	7
3.6	Cuprous oxide	7
3.7	Cuprous oxide as solar cell material	7
3.7.1	Doping of cuprous oxide	9
4	Experimental methods	10
4.1	Sputtering	10
4.2	Hall	13
4.2.1	Temperature dependent Hall	13
4.3	X-Ray Diffractometry	14
4.4	Transmission measurement	20
4.5	Secondary Ion Mass Spectrometry	21
4.6	Experimental equipment and measurement details	23
4.6.1	Hall	23
4.6.2	UV-Vis	23
4.6.3	Sputtering	23
4.6.4	SIMS	23
4.6.5	Laser cutting	23
4.6.6	XRD	23
4.6.7	Scanning electron microscope (SEM)	23
4.6.8	Sample preparation	24
5	Results and discussion	25
5.1	Sputter deposition	25
5.2	As-deposited films	27
5.2.1	Hall	27
5.2.2	XRD	29
5.2.3	UV-vis	34
5.2.4	SIMS	36
5.3	Heat treated films	38
5.3.1	Hall	38
5.3.2	Temperature dependent Hall	41
5.3.3	XRD	43
5.3.4	UV-vis	53
5.3.5	SIMS	54

5.3.6	SEM	57
5.4	Errors and accuracy considerations	64
5.4.1	Hall measurement	64
5.4.2	Comparison of intensity of XRD peaks	64
5.4.3	FWHM and angle positions of XRD peaks	64
5.4.4	UV-vis measurements of heat treated samples	64
5.4.5	Thickness measurement by SIMS	65
5.4.6	Grain sizes from SEM	66
6	Conclusion	67
	References	68

List of Figures

1	Energy band model of dopants in semiconductors: (a) donation of electron from a donor level to the conduction band; (b) acceptance of valence band electrons by an acceptor level, and the resultant creation of holes; Figure adapted from Streetman et al.[1].	8
2	The characteristic glow discharge from the argon gas during sputter deposition of Cu ₂ O thin films. Photo: Martin Nyborg	11
3	Illustration of X-Ray-diffraction between two planes. The figure is obtained from Callister et al.[2]	15
4	Geometric arrangement of an X-ray diffractometer. The figure is obtained from Leng[3].	16
5	Comparison of real diffraction peak (left) and ideal refraction peak (right). Figure adapted from Leng[3].	19
6	SIMS instrumentation. The figure is adapted from Leng[3].	21
7	As-deposited films. From left to right the N ₂ -flow during deposition was 0, 2, 3, 5, 7, 10, 15 and 20 sccm.	26
8	Heat treated films. Upper row: 0 sccm samples. Middle row: 7 sccm samples. Lower row: 20 sccm samples. Left column consists of as-deposited samples, while the next three contain heat treated films at 800°C, 900°C and 1000°C, respectively.	26
9	Resistivity, carrier density and mobility versus N ₂ -flow. The grey symbols represent the 3 sccm film. For most of the values, the error bar have a similar size as the symbol representing them.	27
10	XRD plots of as-deposited samples. Background peaks are indicated with an asterisk (*).	30
11	2θ-value versus N ₂ -flow of Cu ₂ O(111)-, Cu ₂ O(200)- and Cu ₂ O(311)-peak.	32
12	FWHM-value versus N ₂ -flow of Cu ₂ O(111)- and Cu ₂ O(200)-peak.	33
13	Transmittance of as-deposited samples. The 3 sccm sample is shown with a gray dashed line.	34

14	Transmittance of the as-deposited samples as a function of wavelength, zoomed in on the interval where transmittance starts to increase. The 3 sccm sample is shown with a gray dashed line. . .	35
15	Profile of Cu by SIMS	36
16	Carrier density versus heat treatment temperature.	38
17	Mobility versus heat treatment temperature.	39
18	Resistivity versus heat treatment temperature.	40
19	Acceptor energy level, E_a , for different N_2 -flows of 900 °C heated samples.	41
20	Ratio N_d/N_a for different N_2 -flows of 900 °C heated samples. . .	42
21	XRD plots of heat treated 0 sccm samples. Bottom graph: 800°C, middle: 900°C, upper: 1000°C. Background peaks are indicated with an asterisk (*).	43
22	XRD plots of heat treated 7 sccm samples. Bottom graph: 800°C, middle: 900°C, upper: 1000°C. Background peaks are indicated with an asterisk (*).	44
23	XRD plots of heat treated 20 sccm samples. Bottom graph: 800°C, middle: 900°C, upper: 1000°C. Background peaks are indicated with an asterisk (*).	45
24	Full Width Half Maximum of the Cu_2O (200) peak versus RTP temperature for the 0 sccm, 7 sccm and 20 sccm samples.	48
25	Variation of 2θ position of Cu_2O (200) peak with temperature for the 0 sccm, 7 sccm and 20 sccm samples.	49
26	Full Width Half Maximum of the Cu_2O (111) peak as a function of temperature for the 0 sccm and 7 sccm films.	50
27	Variation of 2θ position of Cu_2O (111) peak with temperature for the 0 sccm and 7 sccm samples.	51
28	Intensity variation of the Cu_2O (200) peak with temperature for the 0 sccm, 7 sccm and 20 sccm heat treated samples.	52
29	Transmittance measurements of heat treated samples.	53
30	N profile for 0 sccm heat treated sample.	54
31	N profile for 7 sccm heat treated sample.	55
32	N profile for 20 sccm heat treated sample.	56
33	SEM images of as-deposited and heat treated films of 0 sccm nitrogen flow.	58
34	SEM images of as-deposited and heat treated films of 7 sccm nitrogen flow.	59
35	SEM images of as-deposited and heat treated films of 20 sccm nitrogen flow.	60
36	Profile of Cu by SIMS	65

List of Tables

1	Thicknesses of the thin films as measured by SIMS	36
---	---	----

- 2 Ratio of donor to acceptor concentration, N_d/N_a , and acceptor energy level, E_a , for the samples that were heat treated at 900°C. 41

1 Abstract

In this thesis N doping of Cu_2O has been investigated in thin films deposited by reactive magnetron sputtering. Films with N_2 -flows of 0 sccm, 7 sccm and 20 sccm was heat treated by RTP at 800, 900 and 1000°C for three minutes. The goal has been to produce p+ doped films, with a low resistivity for use in solar cells. The results show that so far, this seems possible to achieve by further investigation.

2 Motivation: Why p+ Cu₂O?

Cuprous oxide, or Cu₂O, is a natural p-type semiconductor with high absorption efficiency and a direct band gap of 2.1eV. Together with the facts that it is non toxic, abundant in nature and cheap and easy to produce this make Cu₂O a good candidate for use in solar cells.

With its bandgap of 2.1 eV and high absorption coefficient, cuprous oxide is a good candidate for the top, absorbing layer of a tandem solar cell. By transmitting light of energy less than 2.1 eV, the bottom layer could then be silicon, which is already established as a solar cell material and has a band gap of 1.1eV. While Cu₂O and Si solar cells alone have maximum efficiencies of about 20% and 29,8%, respectively, combined as a tandem cell a conversion efficiency of 41% could be approached.[4]

Another utilization of Cu₂O could be in a tandem solar cell with ZnO as a top, so called, window layer. However, this design is challenged by a resistive contact to the Cu₂O layer. However, by adding a sheet of p+ Cu₂O in between the contact and the Cu₂O layer, this could be solved. This is a direct motivation for this thesis, in which N-doping of Cu₂O is investigated with the goal of achieving a low resistivity p+ material.

3 Theory

3.1 Energy bands

A solid is a collection of atoms, consisting of a positively charged nucleus surrounded by negatively charged electrons. Because nuclei and electrons are small particles they obey quantum mechanical laws. Their position in space cannot be determined only be determined to a certain probability, which is given by a particle's distribution function. This probability distribution is called a *wave function*, or the quantum state of the particle. It is determined by the type of particle and its boundary conditions.

In a solid the electrons of the atoms are closely spaced. This causes their wavefunctions to overlap. However, by Pauli's exclusion principle two or more electrons cannot occupy the same quantum state. This leads to a shift and split of the different energy levels of the electrons.: From discretely separated energy levels in a single atom the electrons in a solid instead turn into states with a range of closely spaced energy levels, called energy bands.

Every solid has its own characteristic energy band structure.

3.2 Semiconductors

Materials that lead current well are called *conductors*. Materials that do not are called *insulators*. However, there also exists materials that are in between. These are the *semiconductors*, which may be slightly conductive, or they may be conductive under certain conditions, for instance if they are illuminated or heated.

3.3 Crystal structure

Material for this section is obtained from Kittel[5] and Streetman et al.[1].

Solids can be classified in three types according to their degree of structure. In a *single crystal* the atoms are arranged in a symmetric, periodic pattern. The word "single" refers to the fact that one crystal pattern is repeated throughout the whole solid. In other materials there might be different crystal patterns at different locations. Such materials can be seen as a collection of many small single crystals randomly oriented with respect to each other. They are called *polycrystalline* materials. The least ordered material have no long range structure at all and is said to be *amorphous*.

The periodicity of a single crystal can be represented by a symmetric and regular array of points in space called a *lattice*. The lattice is defined by three fundamental translation vectors, \vec{a} , \vec{b} and \vec{c} such that the atomic arrangement looks the same when viewed from point \vec{r} as from point

$$\vec{r} = \vec{r} + \vec{a} + \vec{b} + \vec{c} \quad (1)$$

The lattice is a mathematical abstraction. When a *basis* of one or several atoms is attached to each point, a crystal results.

The crystal structure could be represented by a volume of the lattice which when repeated produces the whole crystal. A volume like this is called a *unit cell*. The smallest possible unit cell is called a *primitive cell*. It contains only one lattice point. One way to define a primitive cell is to draw the smallest parallelepiped possible with one lattice point in each corner. It will then have eight corner points, and each corner point will be shared with eight neighbouring primitive cells. It will thus have $1/8$ effective point per corner, which makes one effective point per cell.

Although the primitive cell is the smallest unit cell, it might not represent the symmetry of the lattice well. Once the primitive cell is found one can define a set of *primitive vectors*, \vec{a} , \vec{b} and \vec{c} , so that when the cell is moved in a direction equal to a multiple of these, an identical primitive cell is found.

One can define a crystal plane by the use of a coordinate system that has its origin in any lattice point and axes along the edges of a unit cell. First, a set of integer coordinates where the plane intersects the coordinate axes is found. The plane can be moved in and out from the origin in order to find such an integral number of intercepts. Then, the reciprocal value is taken of the integral intercepts. Further these are reduced to the smallest set of integers which have the same ratios as the original values. This set of integers, (hkl), then labels the plane.

A direction in a lattice is defined as a set of three integers with the same relationship as a vector in the same direction. The three components are expressed as multiples of the basis vectors of the crystal, and they are reduced to their smallest values which retain the relationship among them.

3.4 Defects and doping

Material for this subsection is obtained from Campbell [6] and Streetman et al.[1].

In an *ideal crystal* all of the atoms are positioned in well-defined, regular lattice sites, and there are no impurities or defects. However, this is never the case in a real crystal at temperature above 0 K. It will then have enough energy present for irregularities, or *defects*, to occur.

Structural defects in a crystal could either be zero, one, two or three dimensional. A zero dimensional defect is limited to one structural lattice site and its immediate vicinity and is termed a *point defect*. One type of point defect is an empty lattice site, which is called a *vacancy*. Another type is an *interstitial*, which is an atom that, instead of occupying a lattice site, occupies the interstitial space in between.

Vacancies and interstitials of a lattice atoms are *intrinsic defects*. The second kind of point defect is *extrinsic defects*, consisting of foreign atoms at interstitial or lattice sites. When a foreign atom occupies a lattice site, it is referred to as a *substitutional impurity*.

The term *defect* is not necessarily negatively connotated. An important way of improving the electrical properties of a semiconductor is by the process of *doping*, in which substitution impurities are introduced into a semiconductor.

Doping provides extra charge carriers in the solid, because substitutional impurities often have an energy state within the band gap that can either serve as a *donor level* or *acceptor level* as illustrated in Figure 1. An extra energy state that is filled with an electron and located near the conduction band edge will easily donate the electron to the conduction band, where it becomes a free carrier. This is termed *n-type doping*. Another type of doping is the *p-type doping*, in which the impurity atom has an empty energy state located near the valence band edge that can capture a valence band electron so that a hole is created.

One usually wants to control the carrier concentration by the doping levels. This is done by having much higher concentrations of dopants than the intrinsic carrier concentration. In this way the intrinsic carrier concentration can be looked away from, and the concentration is essentially equal to the doping concentration. That is, $n_0 \simeq N_d$ for an n-type material and $p_0 \simeq N_a$ for a p-type material.

3.5 Solar cells

3.6 Cuprous oxide

This and the following sections are based on Meyer et al.[7] and Bergum et al.[4].

Cuprous oxide, or Cu_2O , is one of the stable phases of the three well established copper-oxide compounds, the others being Cu_4O_3 and CuO (cupric oxide). Cu_2O is an intrinsically p-type semiconductor with a direct band gap of 2.1 eV. Cuprous oxide is abundant in nature, is non toxic and has low production costs. Together with the fact that it has a high absorption coefficient and a direct band gap of 2.1 eV this make cuprous oxide a good candidate for use in solar cells.

The structure of Cu_2O is cubic, where the copper atoms form a face centered cubic(fcc) lattice, while the oxygen atoms constitute a body centered cubic (bcc) sub lattice.

3.7 Cuprous oxide as solar cell material

The efficiency of Cu_2O as predicted by Shockley–Queisser limit (SQL) is about 20%. However, current experimental data only give efficiencies of about 3%. This means that there is a lot of room of improvement.

According to the SQL, materials with a band gap around 1.4 eV will give the maximum efficiencies for single junction solar cells. Cu_2O with its 2.1 eV band gap will therefore not give maximum efficiencies for single junction solar cells. However, there has not been reported on successful n-type doping of Cu_2O [7], hence homojunction diodes are out of reach. Because of this, the focus has rather been on heterojunction solar cell devices of Cu_2O .

Cu_2O , with its high absorption coefficient and relatively large band gap of 2.1 eV, is a good candidate for being the top, absorbing layer of a heterojunc-

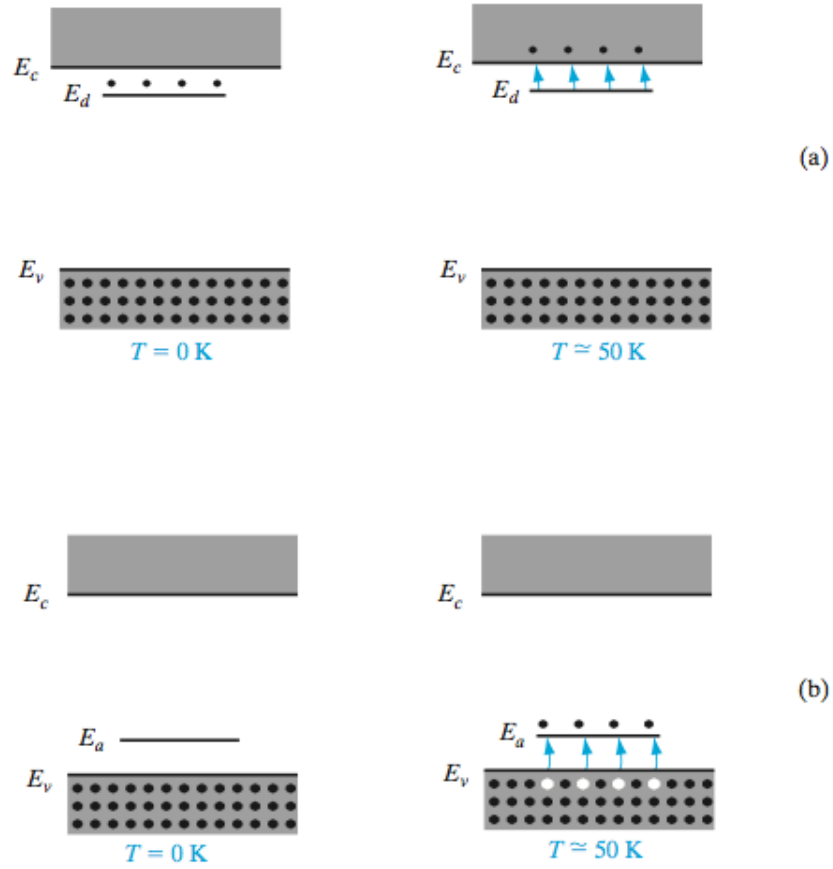


Figure 1: Energy band model of dopants in semiconductors: (a) donation of electron from a donor level to the conduction band; (b) acceptance of valence band electrons by an acceptor level, and the resultant creation of holes; Figure adapted from Streetman et al.[1].

tion solar cell. In combination with ZnO as the n-type transparent conducting window layer.

Because of its bandgap of 2.1 eV cuprous oxide is a good candidate for the top layer of a tandem solar cell with silicon, which has a band gap of 1.1 eV. This tandem cell could theoretically obtain conversion efficiency of 41 % [4].

There has also been attempt to make tandem solar cells with ZnO as top layer and Cu₂O as bottom layer, but this design has challenge with a resistive contact to the Cu₂O layer. However, by adding a sheet of p+ Cu₂O in between the contact and the Cu₂O layer this could be solved, which is one motivation for this thesis.

3.7.1 Doping of cuprous oxide

In order to understand doping of cuprous oxide, one must look at its constituents. Cuprous oxide, or Cu₂O, consists of oxygen and copper having ionic bonds. The copper atoms are ionized to Cu^+ , while the oxygen atoms are ionized as O^{2-} . When Cu₂O is doped with nitrogen, the nitrogen atoms are expected to replace oxygen atoms of the lattice. Nitrogen is a group five element, and is expected to have oxidation number +3 in cuprous oxide, thus acting as an acceptor in the place of oxygen. Thus cuprous oxide is expected to be more p-type with nitrogen doping.

When doping the Cu₂O films with nitrogen the mobility is expected to decrease due to increased lattice scattering by the impurities. But because the carrier concentration will increase, the conductivity is expected to increase, which is equivalent to a decrease in the resistivity of the material.

4 Experimental methods

4.1 Sputtering

Material for this section is obtained from Campbell [?].

Sputtering is a technique, first discovered in 1852 by Langmuir, where energetic particles bombard a solid so that secondary particles are ejected. The material which is bombarded is called a *target*. The energetic particles are usually ions from a plasma.

Common applications of sputtering is etching, secondary ion mass spectrometry and film deposition. The ejected particles are usually not in thermodynamic equilibrium with their surroundings. This causes them to easily deposit if they hit a surface. In thin film deposition a substrate is placed in the vicinity of the target so that particles will deposit and eventually build up. Thus, a thin film can be made of any material that can form a solid target.

When sputtering is used for deposition it has the advantage of making good step coverage. It also induces less radiation damage than electron beam evaporation. Sputtering is also well suited for deposition of compound materials and alloys.

A typical setup consists of a target and a substrate holder in a vacuum chamber. The target is connected to a negatively charged cathode. It is partly covered by a cylindrical shielding, which acts as the positively charged anode. The distance between the shielding and target used for this thesis is 3 mm. The substrate is placed on a substrate holder, which is electrically isolated from the rest of the chamber, which is grounded. The substrate and target are closely spaced, often less than 10 cm, in order to collect as many sputtered atoms as possible. Also, in order to improve the uniformity of the sputtered film, it is common to let the wafer be scanned past or, as in this thesis, rotated below the target.

Figure 2 shows an image of two substrates during sputter deposition of Cu_2O thin films. The characteristic purple color comes from the glowing argon plasma.

The plasma is formed once a voltage of a certain strength is applied between the cathode and anode. It starts when electrons are ejected from the cathode and accelerated away due to the negative potential. Some of the electrons will collide with neutral atoms in the feed gas. Valence electrons may be repelled so that positive ions are formed. The positive ions will then be accelerated towards the negatively charged cathode. If the energy is high enough bonds of the target material will loosen and atoms and diatomic molecules from the target are ejected. The sputtered atoms and molecules may hit the substrate and form a thin film. Often the sputtered atoms have enough energy when hitting the surface too diffuse, leaving an evenly distributed film.

Sputtering is done using either RF or DC voltage. DC sputtering gives larger sputter rates if the target is conductive. However, for non conductive targets the voltage must be RF in order to avoid that charge build up. An RF voltage can also be used for conductive materials.

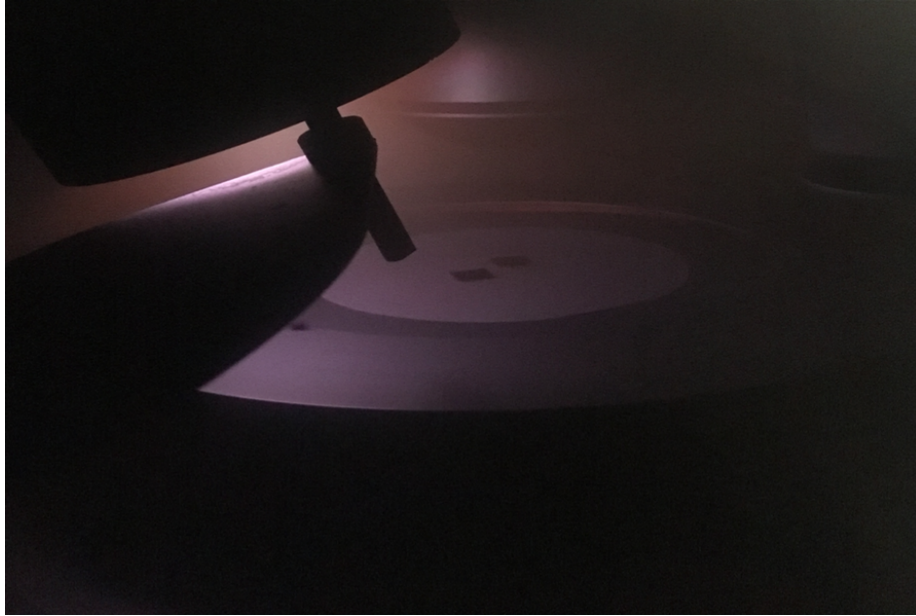


Figure 2: The characteristic glow discharge from the argon gas during sputter deposition of Cu_2O thin films. Photo: Martin Nyborg

A gaseous plasma is a dynamic condition, where neutral gas atoms, ions, electrons and photons exist in a near balanced state simultaneously. Together with neutral atoms and molecules, secondary electrons may be ejected from the target when ions hit. As these are accelerated away they will maintain the plasma by hitting neutral gas atoms so that they become ionized. New ions are accelerated towards the target, and the sputtering process and the plasma is maintained.

The plasma has a characteristic glow, which is a result of non ionizing collisions between electrons and plasma atoms. In collisions with little energy an electron may be captured by an atom giving off its excess energy as a photon.

An important quantity in sputter deposition is the sputter yield, S , which is the average number of target atoms that are ejected for each plasma ion incident. The sputter yield is influenced by the mass of the plasma ions, their energy and of characteristics of the target material, such as its atomic mass and its crystallinity. Sputter yield also depends on the angle at which the ions hit the surface. For crystalline targets the yield will be higher if the ions hit in directions along the low Miller indices.

The higher the energy of the plasma ions, the higher the sputter yield. This holds until a certain value, at which the process changes from sputtering to implantation. If the energy gets below a certain threshold value, no sputtering will occur. For most target materials this lies between 10 and 30 eV.

Although the sputter yield generally increase with the mass of the plasma

ions, it is higher for ions with full or close to full valence shells. Therefore, noble gases are widely used for the plasma.

The higher the sputter yield, the faster the *deposition rate*, R_d . This has the dimensions of thickness per time, usually nanometres per minute. A simple model for the deposition rate is

$$R_d = \frac{J_{ion} * S * E_T}{\rho/m} \quad (2)$$

, S : Sputter yield, J_{ion} : Ion flux to the target, E_T : Transport efficiency, i.e. proportion of sputtered particles reaching the wafer, ρ : Mass density, m : Mass

The numerator is equal to the flux of sputtered atoms reaching the wafer. When divided by the number density this produces the deposition rate.

For closely spaced systems the transport efficiency, E_T , is typically assumed to be fairly close to one.

A plasma is a gas that in substantial part is ionized. Plasma can be used in the place of high temperatures to crack molecules, and thus drive some chemical reaction. It can also be used to create ions and accelerate these. A plasma is initiated when a large voltage is applied across a gap containing a low pressure gas.

When depositing insulating materials, an RF plasma must be used. DC sputtering is usually favoured when elemental metals are to be deposited due to its large sputter rates.

4.2 Hall

4.2.1 Temperature dependent Hall

When doping a material, it is desirable to know if the dopants have been successfully incorporated into the sample. In a regular Hall measurement, which is done at one temperature only, the carrier concentration is recorded. However, it is not known where the carriers come from.

In general, a semiconductor can contain several types of impurities at once, both acceptors and donors. Whether it is an n or p type conductor is determined by which kind of dopant is the most present.

In many situations it is useful to not only know the carrier concentration, but also how many electrically active impurities there are in the sample. In this way one can see if the number of carriers only have contribution from the intentional dopants or if maybe there are some compensating impurities available.

In temperature dependent Hall measurement the Hall coefficient, R_H , which is directly related to the carrier density, is measured as a function of temperature.

If one assumes a non-degenerate semiconductor, in which $E_F - E_v \geq 3kT$, the hole density, p , obeys the equation:

$$p^2 + p(N_d + N'_v) - (N_a - N_d)N'_v = 0 \quad (3)$$

$$, N'_v = \beta N_v e^{-(E_a - E_v)/kT}$$

When plotting the natural logarithm of carrier concentration, $\ln(p)$, versus the inverse temperature, $1/T$, the graph will be linear with a negative slope proportional to the acceptor energy level, E_a . At a certain temperature, however the graph will reach a plateau value, which happens when all the dopant atoms are ionized and the carrier concentration from the dopants do not longer increase with T . (See Figure 3-18, Streetman.)

When TdH data are fitted to this plot of the natural logarithm of p versus $1/T$, one can determine the ionization energy of the acceptors, which equals their energy level above the valence band edge, given by E_a , the ratio of the donor concentration to acceptor concentration, N_d/N_a , and the difference between acceptor concentration and donor concentration, $N_a - N_d$. Together the last two expressions give the donor and acceptor concentrations, N_d and N_a . The acceptor level relative to the valence band edge, E_a , is proportional to the slope of the linear part of the curve. The ratio of donor to acceptor concentration, N_d/N_a , is given by the point where the curve intersects the $1/T$ -axis. The difference between acceptor concentration and donor concentration, $N_a - N_d$, is determined by where the curve intersects the y-axis after sloping off.

4.3 X-Ray Diffractometry

Material for this section is obtained from Chapter 2 in Leng[3] and Chapter 3 in Callister et al.[2].

X-Ray Diffractometry (XRD) is the most widely used X-ray diffraction technique. It is used for determining the structure of a crystalline material, which also reveals its chemical compounds. The technique builds on the phenomenon of wave interference as X-ray radiation is refracted from crystal planes of a specimen.

Two electromagnetic waves travelling in the same direction with the same wavelength, can either reinforce or cancel each other, depending on their phase difference. If the phase difference equals an integer number of wavelengths, constructive interference occur. However, if it equals an integer number of half the wavelength, destructive interference will occur.

Figure 3 illustrates diffraction of X-ray waves by two equal and parallel crystal planes. The incoming waves, 1 and 2, are monochromatic and in phase. If also the outgoing waves, 1' and 2', are in phase, constructive interference will occur. The phase difference of the beams depends on their difference in path length of travel. For constructive interference to occur, it must equal an integer number of wavelengths. As seen from the figure, the path difference between the waves is given by $SQ + QT$. By observing that $SQ = QT = d * \sin\theta$, the condition for constructive interference can be formulated as Bragg's law:

$$2 * d_{hkl} * \sin\theta = n\lambda \quad (4)$$

, where $n \in \mathbb{N}$ and d_{hkl} is the spacing of the planes.

Bragg's law expresses that constructive interference between diffracted waves, depends on the distance of the crystal planes, d_{hkl} , and the incoming angle, θ , of the beam relative to the planes. In an XRD measurement diffracted intensity is recorded for a range of incoming angles, resulting in a number of intensity peaks located at different angles. Each peak represent diffraction from a certain crystallographic plane. Because different crystalline materials have different types of crystal planes, with different lattice parameters, a diffraction spectrum provides a fingerprint of the sample.

Figure 4 shows the geometric arrangement of an X-ray diffractometer. X-ray radiation is generated in an X-ray tube, and passed through slits which assures a slightly divergent beam at the sample. The radiation is diffracted by the sample and form a convergent beam at the receiving slits before entering the detector. A monochromatic filter must be used before detection. This is commonly placed in the diffracted beam path rather than in the incoming beam path. In this way background radiation from the sample is suppressed as differing wavelengths are filtered. During measurement the detector, X-ray tube and sample are moved relative to each other in order to obtain refraction intensities at a range of 2θ values.

The original use of XRD was for examination of crystalline samples in powder form. From this, a data base containing diffraction spectra of more than

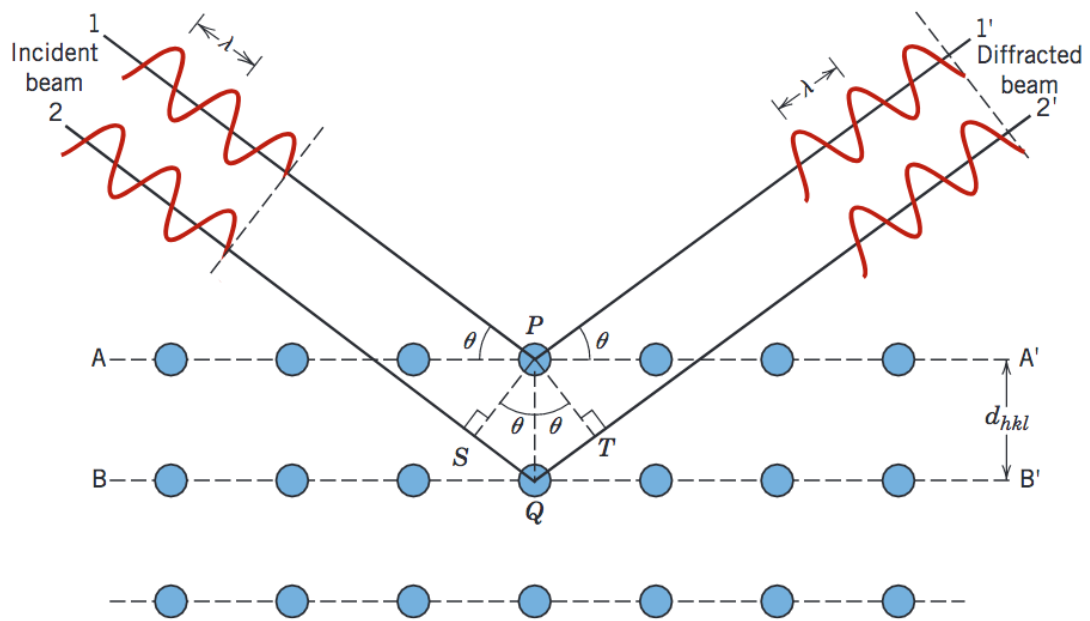


Figure 3: Illustration of X-Ray-diffraction between two planes. The figure is obtained from Callister et al.[2]

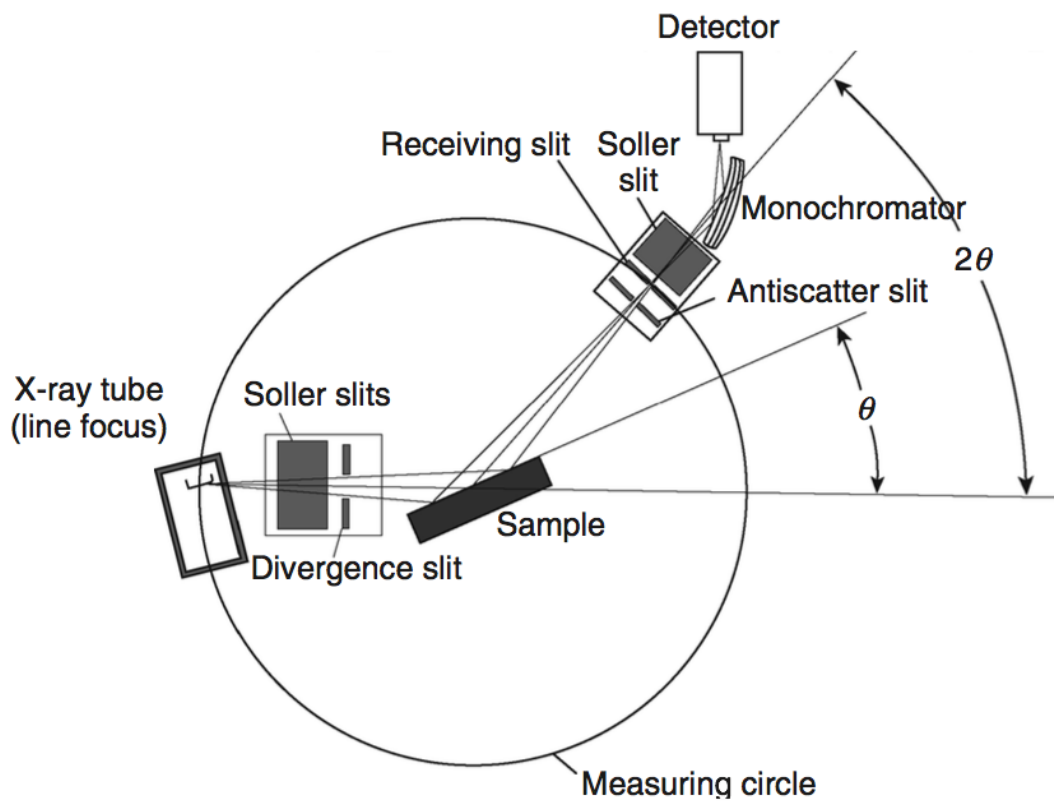


Figure 4: Geometric arrangement of an X-ray diffractometer. The figure is obtained from Leng[3].

60 000 substances in powder form exists. By matching an obtained peak spectrum with that of a standard, the crystalline substances of a sample can be identified. However, powder substances have a perfectly random orientation of their crystal planes, which is rarely the case in solid samples. Because of this, one should be aware that the relative intensities among peaks can differ from those of a standard spectrum. A preferential orientation could even make certain peaks disappear. Ideally, the samples of an XRD measurement should be polycrystalline, with a large number of randomly oriented grains.

When conducting an XRD measurement the choice of 2θ range, X-Ray radiation and step width for scanning is important in order to obtain data of sufficient quality. The 2θ range should be large enough to make detection of all relevant planes possible. The X-Ray radiation should have a wavelength that is able to detect all the planes, and the step width for the 2θ scan should be chosen right. If the step width is very small, shifts of the peaks may occur. If it is too big, however, the peak intensity can be suppressed. A rule of thumb is to use a step width that allows ten to twenty individual data points over a peak's *Full Width at Half the Maximum* (FWHM), which is marked as B to the left in Figure 5.

Recorded diffraction peaks always have a certain width, although for a single crystal it should ideally have the peak of a delta function, as illustrated in Figure 5.

The widening of a peak is typically caused by the phenomenon of *incomplete destructive interference*. According to Bragg's law constructive interference only occur when the deflected beams of neighbouring planes have a path difference equal to an integer number of wavelengths. For a given plane spacing, d , this happens at a certain angle, the *Bragg angle*. Conversely, if the path difference between neighbouring planes equals an integer number of half wavelengths, destructive interference occur, which will also only happen at a certain incoming angle. For beams at other angles than these two, diffracted waves of adjacent planes will both reinforce and destruct each other. However, the distance between two planes of further separation than neighbouring planes might give just the right path difference for destructive interference to occur, as the difference in length travelled increase with the distance between planes. This means that for incoming angles close to the the Bragg angle, destructive interference will occur between waves that are diffracted from two crystal planes far apart. For each shallow lying plane of the crystal, there exist a deeper plane for which a deflected wave will have travelled a path difference that gives destructive interference. However, the thickness of a sample might be too thin for this deeper laying plane to exist, or the sample might have crystallites that are too small to contain enough planes. Instead the beam will not be cancelled, giving rise to a broadening of the intensity peak.

Another case where incomplete destructive interference leads to a broadening of intensity peaks, is when the incoming X-ray beam is not perfectly parallel, which is always the case in an XRD measurement. As a result, a variation in the angle with a certain crystal plane occur, which means that constructive interference will occur for an intervall around the Bragg angle. The same ef-

fect causes incomplete destructive interference to happen for randomly oriented grains in a polycrystalline material. The different orientations of the grains result in different incoming angles for the same type of plane, and so a broadening of the intensity peak occur. This effect gets bigger, the smaller the size of the crystallites.

Even though the Bragg condition is satisfied for a certain plane and incoming angle, the diffraction intensity may not be the same for different planes. In order to understand this, it is useful to look closer at what happens in the process. X-ray diffraction in a crystal arises from X-ray scattering by individual electrons in the atoms of the crystal. The electrons scatter the incident beam to all directions in space. The intensity of a scattered X-ray from an electron depends on the intensity of the incoming X-ray, the distance the scattered beam has travelled from the material, the properties of the crystal atoms and the angle between the incoming beam and the scattering direction. The angle dependency of the intensity, even if the Bragg condition is assumed to be fulfilled, is because the reflected beam is polarized during the scattering process.

However, even if the intensity of the scattered radiation from each electron is known, the intensity of the total scattered beam is not simply the sum of contributions from each electron. This is because electrons have different positions in an atom, which gives rise to destructive interference for any nonzero scattering angle.

The most important factor that affects the scattered intensity is so called *structure extinction*, in which constructive interference between certain planes is cancelled due to destructive interference with other planes. If a crystal contain multiple chemical elements, the diffraction intensity is usually not extinguished by this process, but reduced.

In addition to peak widening, shift in the 2θ position peaks might occur. This happens when there is residual stress in the sample, which causes a change of the lattice parameters. For example, a tensile stress that increases the spacings will shift a peak to lower 2θ value. On the other hand, compression stress causing the spacings to decrease will shift the position to a higher 2θ value. If nonuniform strain is present, both contraction and expansion of the spacings might occur, causing widening of the peak.

X-rays are used because they have wavelengths smaller than the interatomic spacings in a crystal, which is necessary for the detection of different planes.

X-rays are produced in an *X-ray tube*, where electrons are accelerated and collide with a metal target. The rapid deceleration of electrons that hit the target results in conversion of their kinetic energy into X-ray radiation of a range of wavelengths. Radiation is also produced by a second mechanism, when incident electrons have enough energy to excite target electrons from their inner shell. The empty state left behind will then be filled by an electron from a higher energy shell, emitting an X-ray with corresponding wavelength in the process. This kind of *characteristic X-ray* is specific for the target material used. In XRD measurements the X-ray beam must only consist of waves with one wavelength and one of the characteristic X-rays is chosen. Other wavelengths are filtered out.

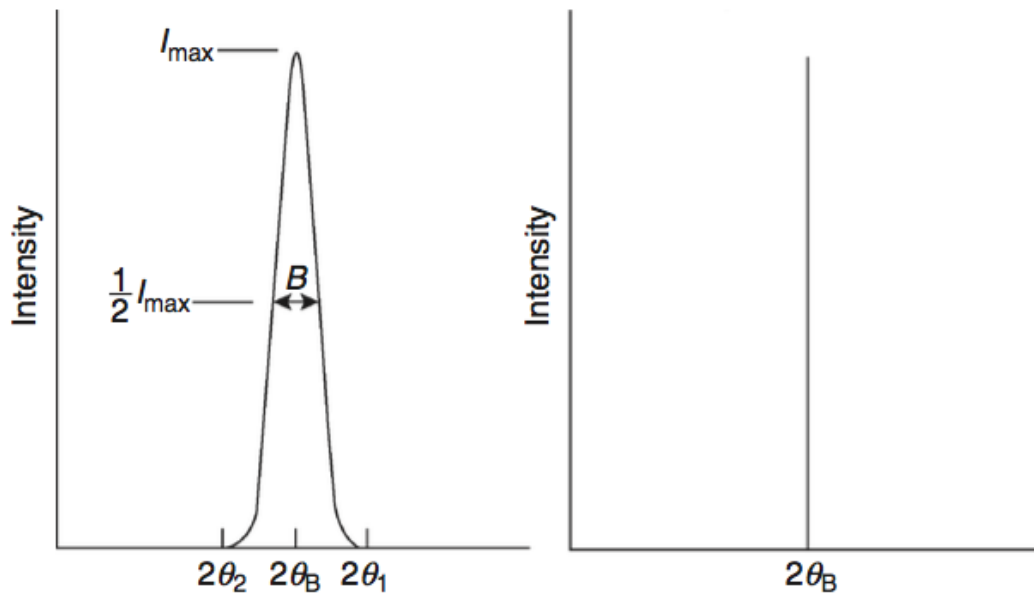


Figure 5: Comparison of real diffraction peak (left) and ideal refraction peak (right). Figure adapted from Leng[3].

4.4 Transmission measurement

As the cuprous oxide thin films are intended for solar cells, it is interesting to look at their transmission properties. Any semiconductor is expected to have a high absorption of electromagnetic waves with a frequency corresponding to the energy of the band gap or higher.

The optical band gap can be obtained by fitting a Tauc plot model based on Equation 5.

$$\alpha h\omega = B(h\omega - E_g)^m \quad (5)$$

, α : Absorption coefficient

, E_g : Optical band gap

, ω : Angular frequency

, h : Planck's constant

, B : Constant

, m : Constant equal to 1/2 if the band gap is direct, and equal to two if it is indirect

4.5 Secondary Ion Mass Spectrometry

Material for this section is obtained from Leng[3] and Campbell[6].

Secondary ion mass spectrometry (SIMS) is a technique for compositional analysis of a material's surface region. A beam of energized *primary ions* bombard a small area of the examined material. As a result *secondary ions* are sputtered, which can be detected and analyzed by a mass spectrometer revealing their elemental identities.

An advantage of SIMS is the ability to detect all elements, including differentiation between isotopes. Several species can be measured during the same run if their secondary ions have the same type of electric charge. Concentrations as low as sub parts per million (ppm) can be detected, under ideal circumstances even sub parts per billion (ppb = 10^{-9}) or smaller. This makes SIMS a great technique for impurity detection. Finally, little or no sample preparation is required.

Figure 6 shows a typical setup for SIMS. A primary ion system, consisting of an ion source, a purifying filter and a deflector make sure that the surface to be analyzed is hit at a certain position and angle by a focused primary ion beam having a specific kinetic energy. The ion beam produce sputtering of secondary particles. The ions of interest typically comprise about 1%. These are extracted and then separated according to their ratio of mass to electric charge. This ratio is counted by a detector, producing an intensity for each element that may be plotted in a mass spectrum.

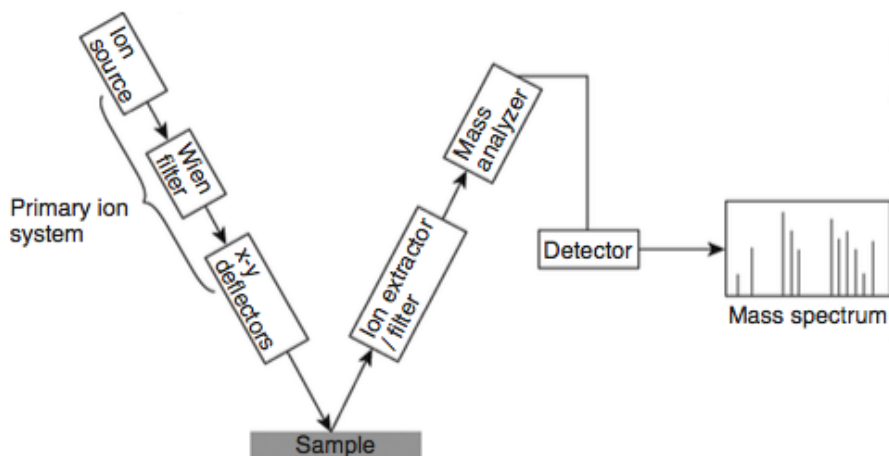


Figure 6: SIMS instrumentation. The figure is adapted from Leng[3].

Although the recorded intensity for an element is proportional to its concentration, conversion between those two is not straight forward. The intensity depends on the sputter yield, the ionization efficiency, collection efficiency and

detector sensitivity. These quantities can vary from day to day and run to run. Further, ionization efficiency and sputter yield vary with element and type of chemical bond. In order to solve this it is common to make a calibration sample for each impurity with known concentration profiles. By measurement of these immediately before or after the data collection, conversion from intensity to concentration is possible.

In this thesis the samples were measured by *dynamic* SIMS. The flux of primary particles is then high, typically greater than $1 \mu\text{Acm}^{-2}$, which makes removal of many atomic layers possible. As a result, one can obtain a depth profile for each element. The intensity is recorded versus time, but the time can be converted into depth by assuming a constant corrosion rate and measuring the crater afterwards. Even though initially the various elements show different sputter rates, a uniform rate is achieved after some time.

Dynamic SIMS destroys the sample. However, the measurement is only done in a small area. Usually this is between $10 \times 10\mu\text{m}^2$ and $500 \times 500\mu\text{m}^2$.

4.6 Experimental equipment and measurement details

4.6.1 Hall

Room temperature Hall measurements and temperature dependent Hall measurements were done by a LakeShore 7604 instrument using Van der Pauw configuration. The carrier mobility, μ , carrier density, N , and resistivity, ρ , was determined. Contacts were made by soldering Ag wires onto the corners of the samples by In contacts.

The temperature dependent Hall measurements were conducted by Heine Nygard Riise.

4.6.2 UV-Vis

A Shimadzu SolidSpe-3700 DUV UV-VIS spectrophotometer was employed in the spectral range of 290 nm to 1500 nm in an integrating sphere setup to determine transmittance.

4.6.3 Sputtering

The Cu_2O thin films were deposited by a Semicore TriAxis Magnetron sputtering system. The target was a circular copper plate, 3 inches in diameter and 0.25 inches thick. The distance between target and substrate was 10 cm.

4.6.4 SIMS

SIMS measurements were done by Alexander Azarov at University of Oslo by a Cameca IMS-7f microanalyzer. The primary ions beam consisted of 15 keV Ce^+ ions. Intensity was converted to concentration by comparison with implanted Cu_2O .

4.6.5 Laser cutting

A Rofin laser cutter were used for cutting the quartz samples. It was run with a frequency of 15 kHz, current of 25 A, a speed of 200 mm/s and an execution count of 20 scribes. The line width was 0.080 mm and the pulse width was 1.0 μm .

4.6.6 XRD

X-Ray Diffraction characterization was performed by a Bruker AXS D8 Discover using a $\text{Cu K}\alpha$ radiation source with two slightly different wavelengths: $\lambda_{\text{K}\alpha_1} = 1.5406 \text{ \AA}$ and $\lambda_{\text{K}\alpha_2} = 1.5444 \text{ \AA}$. The scan was done with 2θ ranging from 30° to 80° with step length of 0.005° .

4.6.7 Scanning electron microscope (SEM)

SEM images were taken by Raj Kumar at FERMIo, University of Oslo. A FEI Quanta 200 FEG-ESEM system was used.

4.6.8 Sample preparation

Double-sided polished 500 μm thick quartz wafers and silicon wafers have been used as substrates for the deposited Cu_2O films. Si was only intended for thickness measurements by ellipsometry. However, the optical conditions in the N doped Cu_2O films turned out to not be comparable with those for undoped Cu_2O , which was the reference. Therefore SIMS measurements were considered more accurate for thickness measurements, and the films deposited on silicon were not used.

The 3 inch wafers were cut by laser ablation into $1 * 1\text{cm}^2$ and $1 * 2\text{cm}^2$ squares.

The quartz substrates were cleaned in two steps. First, the substrates were cleaned with isopropanol in order to remove organic contaminants and particles. Then the samples were cleaned in a piranha solution, which removes organic residues.

The silicon samples were rinsed by RCA1 and RCA3 by Per Lindberg. Right before sputter deposition they were put in a dilute solution of HF acid, also referred to as RCA2, for at least ten seconds in order to remove the native oxide on the surface.

After each cleaning step the substrates were rinsed in deionized water and dried with an N_2 gas flow.

5 Results and discussion

5.1 Sputter deposition

A series of N doped cuprous oxide thin films were sputtered by reactive magnetron sputtering, using argon as a feed gas and a copper target. Oxygen and nitrogen gas were led into the chamber during deposition. In all, eight depositions were performed, with a nitrogen gas flow of 0 sccm, 2 sccm, 3 sccm, 5 sccm, 7 sccm, 10 sccm, 15 sccm and 20 sccm, respectively. For each deposition the oxygen flow was 4.40 sccm, as this value was found to give Cu_2O structure of good quality through calibration depositions in advance. The amount of argon was changed for each N-flow so that the total amount of gas was held at 50 sccm. Deposition time was 30 minutes. The deposited films can be seen in Figure 7.

The order of the depositions was not strictly done with ascending amount of N_2 -flow, as this was not considered important at the time. The first deposition had an N_2 -flow of 3 sccm. Then the reference with zero N_2 -flow was deposited subsequently, after which the films were deposited with ascending amount of N_2 -flow. However, the SIMS results reveal a substantial amount of nitrogen in the reference sample, especially at the bottom of the film. As there was no nitrogen flow during this deposition, the nitrogen content probably comes from remaining nitrogen in the chamber after the deposition with N_2 -flow of 3 sccm.

After the films had been deposited, the samples were characterized by different techniques in order to investigate their structural, electrical and optical properties. These methods were X-Ray Diffraction (XRD), Hall measurement, Transmittance measurement and Secondary Ion Mass Spectrometry (SIMS) measurement.

Some of the deposited samples were also heat treated, in order to see how this would affect their properties. This was done with the samples of N_2 -flows 0, 7 and 20 sccm. The heat treatment was conducted by Rapid Thermal Processing (RTP) at three different temperatures: 800, 900 and 1000 °C, lasting for three minutes. Afterwards the films were characterized by the same methods as before, in addition to temperature dependent Hall (TdH) and Scanning Electron Microscopy (SEM) measurements. The heat treated films can be seen, together with their as-deposited counterparts, in Figure 8.

In the following sections the characterization results are presented for the as-deposited and heat treated samples respectively. The results of the 3 sccm film has been removed or marked differently than the rest. This is because characterization revealed that this was not comparable to the rest of the thin films, as it was much thinner than the other films. The reason for this is not completely clear, but change in the sputtering parameters might be an explanation.

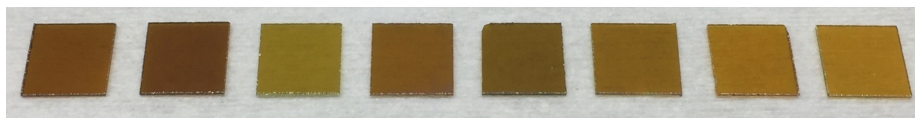


Figure 7: As-deposited films. From left to right the N-flow during deposition was 0, 2, 3, 5, 7, 10, 15 and 20 sccm.

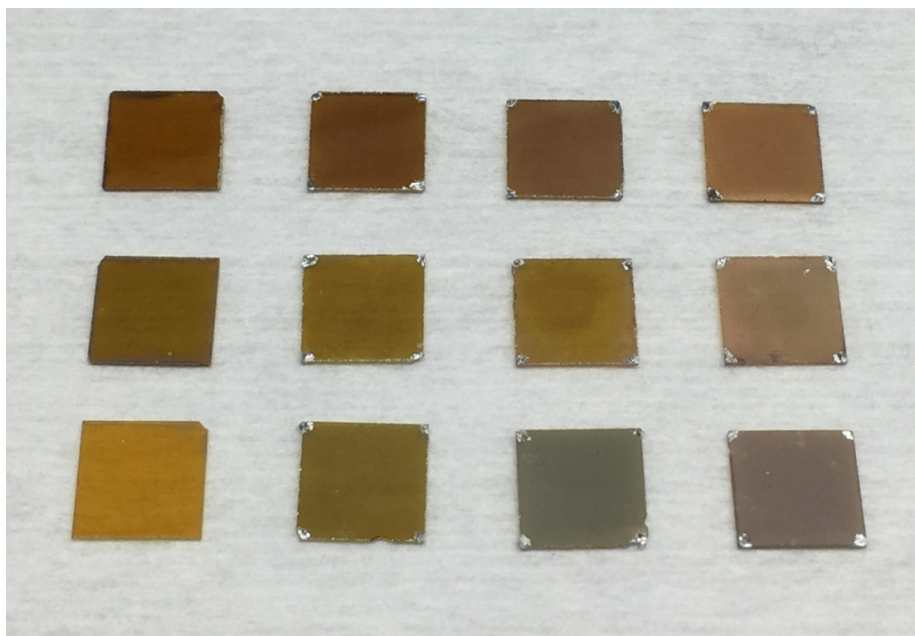


Figure 8: Heat treated films. Upper row: 0 sccm samples. Middle row: 7 sccm samples. Lower row: 20 sccm samples. Left coloumn consists of as-deposited samples, while the next three contain heat treated films at 800°C, 900°C and 1000°C, respectively.

5.2 As-deposited films

5.2.1 Hall

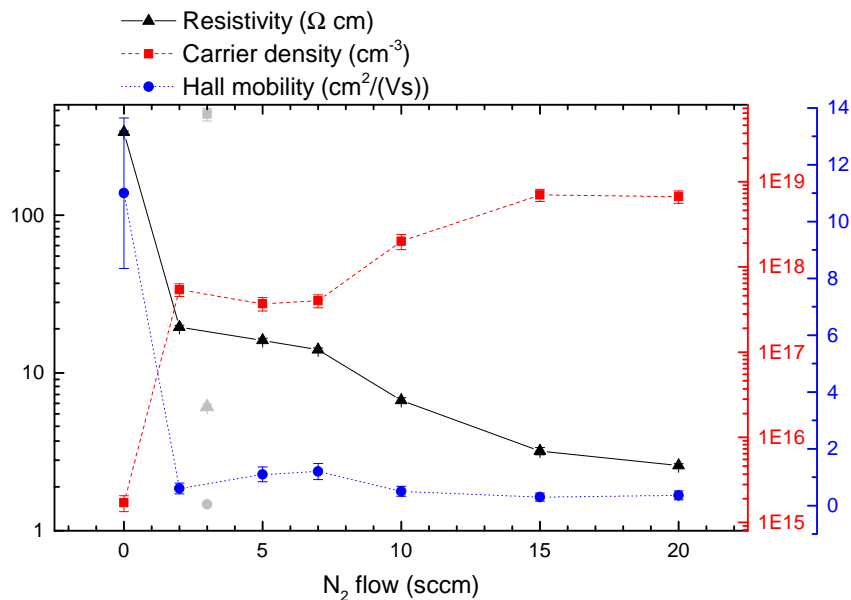


Figure 9: Resistivity, carrier density and mobility versus N₂-flow. The grey symbols represent the 3 sccm film. For most of the values, the error bar have a similar size as the symbol representing them.

Hall measurements were done in order to determine the the resistivity, carrier density and mobility of the films. The thicknesses of the films as measured by SIMS were used to calculate these values.

In Figure 9 the resistivity, carrier density and mobility versus N₂-flow can be seen. The 3 sccm film is represented with gray symbols, not connected with the rest. It is seen that the resistivity decrease with N₂-flow, while the carrier density increase. The mobility has a value of about 11 for the reference film, while for the rest it is around 1cm²/(Vs). It does not have a clear trend with N₂-flow for the films with non zero N₂-flow, but this could be due to the fact that the Hall measurement is not very accurate at measuring mobilities as low as 1cm²/(Vs). This is as expected when doping with nitrogen.

The highest value of resistivity is 334.5 Ωcm, for the 0 sccm film, while the 20 sccm sample has the lowest value of 2.59 Ωcm.

The carrier density is 1.7 × 10¹⁵ cm⁻³ in the reference sample, while the rest of the films have values ranging from 3.7 × 10¹⁷ cm⁻³, in the 5 sccm film up to 7 × 10¹⁸ cm⁻³. In other words, the carrier density increase by a factor between 100 and almost 10000 when deposited with an N₂-flow compared to when not.

The only place where the carrier concentration decrease with N₂-flow, is from the 2 sccm to the 5 sccm sample. The 2 sccm film has a carrier concentration of $5.4 * 10^{17} \text{ cm}^{-3}$, while the 5 sccm sample has a density of $3.7 * 10^{17} \text{ cm}^{-3}$. This a decrease even within the error bars, however a relatively small one. The 7 sccm sample has an even small variation in carrier density compared to the 5 sccm film, with the value of $4 * 10^{17} \text{ cm}^{-3}$, compared to $3.7 * 10^{17} \text{ cm}^{-3}$.

5.2.2 XRD

XRD was employed in order to ensure phase purity in the deposited films. The following XRD data were measured with 2θ -angle ranging from 30° to 80° . The XRD patterns were compared with those of reference spectra of cuprous oxide (Cu_2O) cupric oxide (CuO) and metallic copper, as well as substances containing both copper and nitrogen. However, neither pure metallic copper or combinations of copper and nitrogen were seen in any of the films.

Before the spectras were plotted, the background signal has been removed. However, some peaks which do not belong to the samples remain. These are background peaks.

Normalization of the intensities have been performed, as the base signal was varying a lot from sample to sample. Before normalization, the background peak from the sample holder located at $2\theta = 65.4^\circ$ varied between 2122 and 2987 counts. However, even though the plots have been normalized, comparison of intensity values among different N-flows is not possible, due to the different thicknesses of the samples, which affect the signal. Intensity spectra were normalized after the spectrum of the 5 sccm sample, which have the highest reference peak at $2\theta = 65.4^\circ$. After the background was removed this intensity was of 2987 counts. Thus, by normalizing the XRD spectras, a maximum intensity base signal is obtained for all samples.

The XRD measurement was conducted by both $\text{Cu } \kappa\alpha_1$ and $\text{Cu } \kappa\alpha_2$ radiation, having slightly different wavelengths. Because of this, a splitting of the intensity peaks occur, especially for higher 2θ values. When the intensity values have been read, the left peak has consequently been chosen.

Figure 10 shows the XRD plots of the as-deposited samples. The gray graph belongs to the 3 sccm sample and will not be emphasized.

As seen from Figure 10, the main intensity peaks of the XRD spectra correspond to Cu_2O (111) and (200) orientation for all N_2 -flows. The relative intensity of these two peaks varies between the samples, indicating a variety in preferential crystal orientation. However, this does not seem to depend on the N_2 -flow.

Figure 11 shows the variation in 2θ -position for the $\text{Cu}_2\text{O}(111)$ -, $\text{Cu}_2\text{O}(200)$ - and $\text{Cu}_2\text{O}(311)$ -peaks with N_2 -flow. The 3 sccm sample is not included. It is seen that the 2θ -position of the peaks tend to decrease with N_2 -flow. This is the case for the $\text{Cu}_2\text{O}(200)$ -peak for all the samples, and for the $\text{Cu}_2\text{O}(311)$ -peak for most of the films, the increase from 7 to 10 sccm and from 15 to 20 sccm being exceptions.

The $\text{Cu}_2\text{O}(111)$ -peak has not an equally clear trend. It increases when the N_2 -flow increases from 0 to 2 sccm, from 5 to 7 sccm and from 15 to 20 sccm, and decreases for the rest. However, the decreases in 2θ -position are generally larger than the increases.

A decrease in the 2θ -position of the peaks with N_2 -flow is equivalent to an increase in the distances of the crystal planes. This is expected when nitrogen substitute oxygen in the lattice, as a nitrogen atom has bigger radius than an

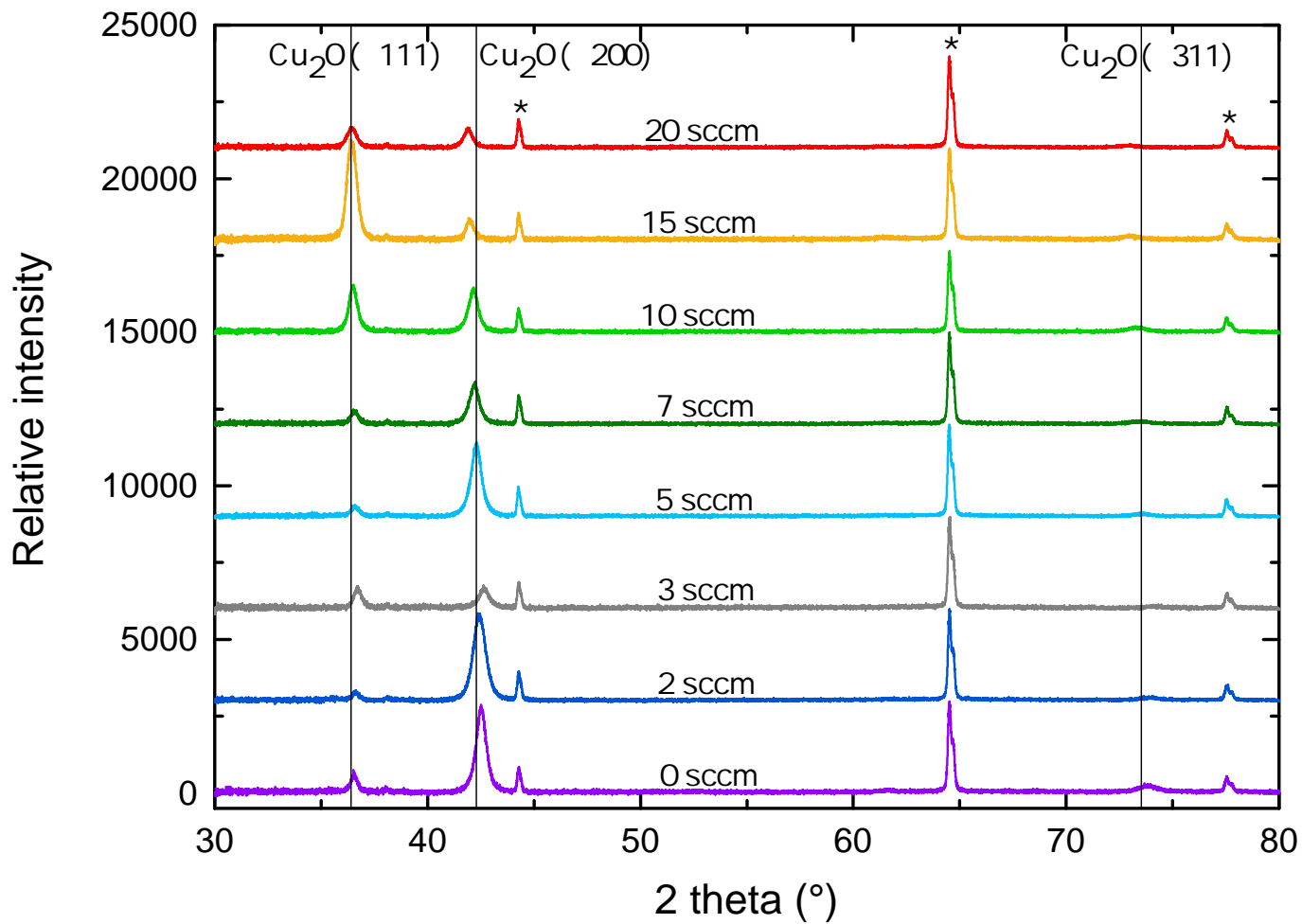


Figure 10: XRD plots of as-deposited samples. Background peaks are indicated with an asterisk (*).

oxygen atom. The lattice parameters may also change due to stress and strain of the crystal planes, which is expected to occur in deposited films. This can explain why the 2θ -position for some samples and crystal orientations increase with N_2 -flow.

In Figure 12, the FWHM-values of the $Cu_2O(111)$ - and $Cu_2O(200)$ -peak is plotted versus N_2 -flow. The figure shows that the FWHM-value of the $Cu_2O(111)$ -peak either is constant or increasing with N_2 -flow. The FWHM of the $Cu_2O(200)$ -peak on the other hand, mostly decrease with N_2 -flow. The values for the $Cu_2O(311)$ -peak are not plotted, as the values are uncertain due to its low intensity.

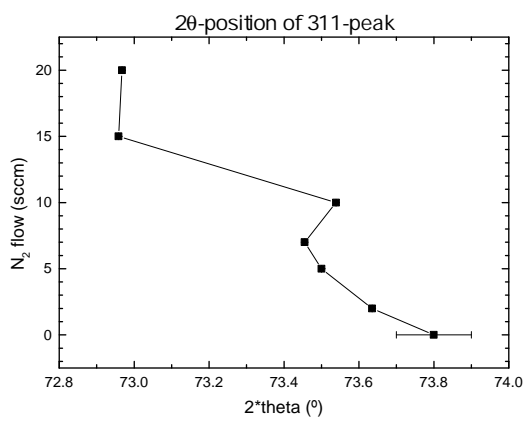
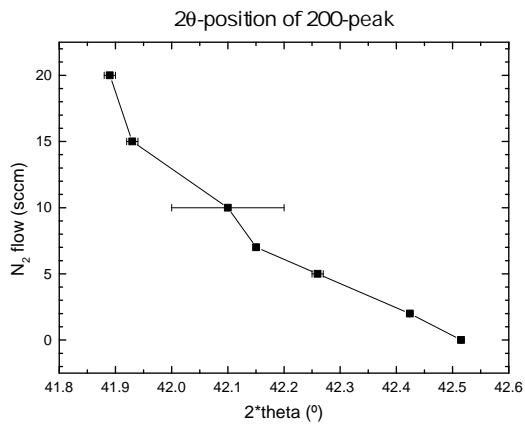
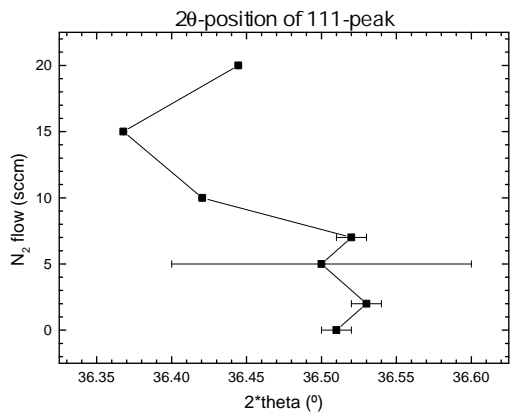


Figure 11: 2θ-value versus N₂-flow of Cu₂O(111)-, Cu₂O(200)- and Cu₂O(311)-peak.

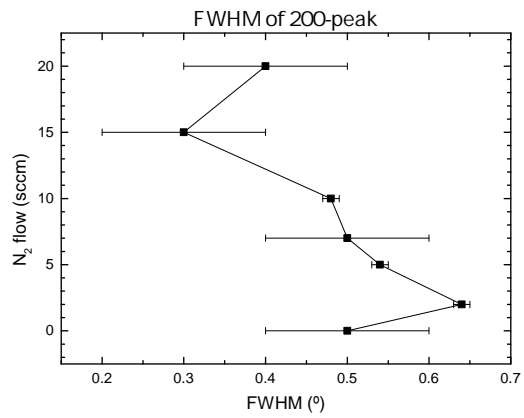
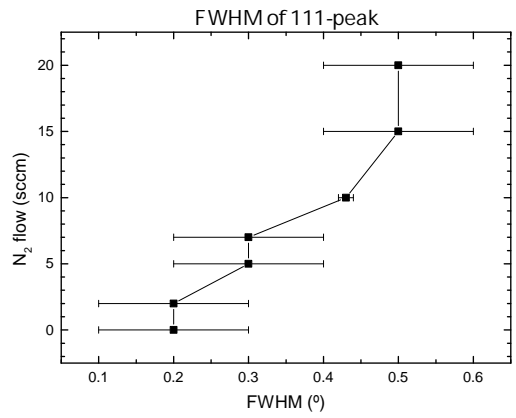


Figure 12: FWHM-value versus N₂-flow of Cu₂O(111)- and Cu₂O(200)-peak.

5.2.3 UV-vis

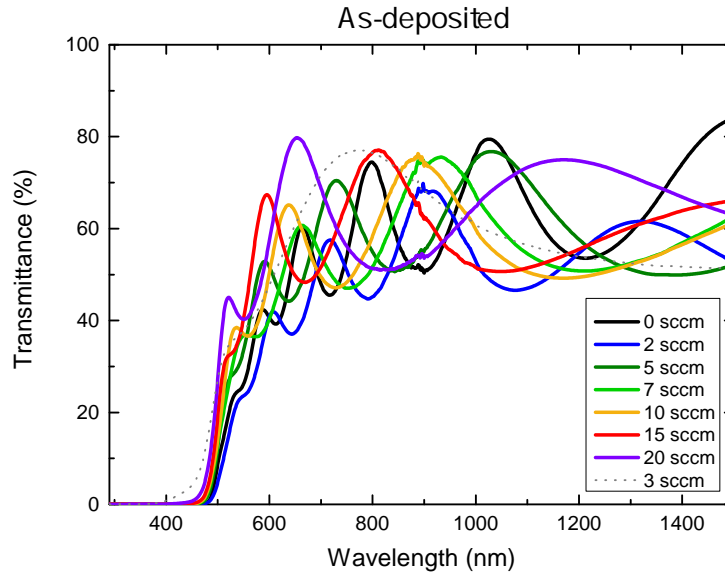


Figure 13: Transmittance of as-deposited samples. The 3 sccm sample is shown with a gray dashed line.

Figure 13 shows transmittance measurements of the as-deposited samples. One can see that there is almost zero transmittance in the wavelength range of 290 nm to about 470 nm, which corresponds to energies below the band gap of the films, indicating a high absorption in this area. For wavelengths above 470 nm, the transmittance increases substantially, reaching values that roughly varies around 60%. It does not seem to be any dependence of the transmittance with N_2 -flow.

In Figure 14 the transmittance plot of Figure 13 has been zoomed in on the area where the transmittance starts to increase. It looks as if the transmittance starts to increase at lower wavelengths the higher the N_2 -flow. If this is true, it is an indication of increase in the optical band gap with N_2 -flow. However, this is only an indication of how the optical band gap behaves with increasing N_2 -flow, as it is hard to look from the transmittance plot exactly at which wavelength transmittance starts to occur.

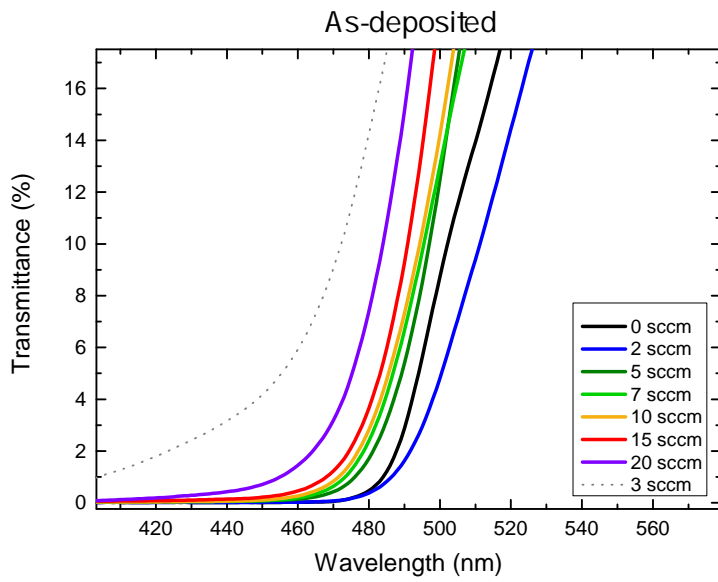


Figure 14: Transmittance of the as-deposited samples as a function of wavelength, zoomed in on the interval where transmittance starts to increase. The 3 sccm sample is shown with a gray dashed line.

5.2.4 SIMS

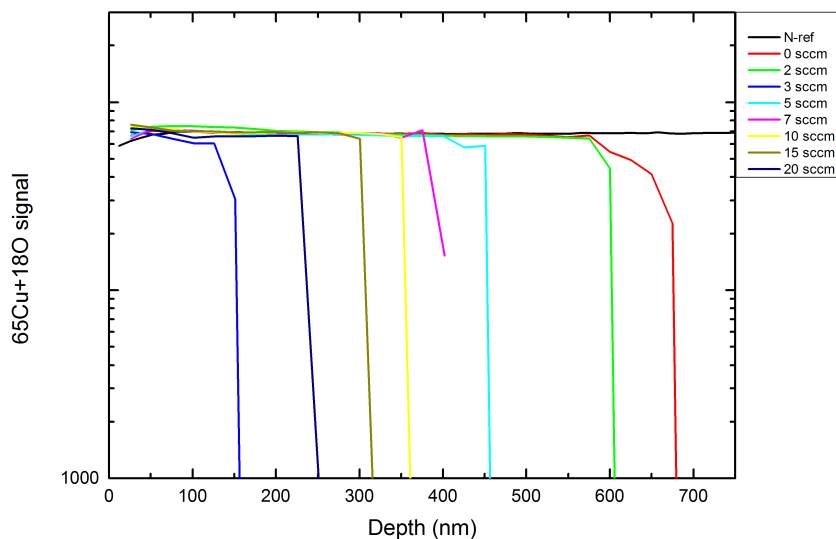


Figure 15: Profile of Cu by SIMS

Table 1: Thicknesses of the thin films as measured by SIMS

N ₂ -flow	Thickness (nm)
0	675
2	600
3	150
5	450
7	400
10	350
15	300
20	225

SIMS measurements were conducted in order to estimate the nitrogen concentration and thickness of the films.

The thicknesses obtained are seen in table 1. When looking away from the 3 sccm sample, the thicknesses decrease with N₂-flow, varying from 225 nm in the 20 sccm film, to 675 nm for the reference film. This is as expected, as the sputter rate decreases when sputtering with nitrogen.

Figure 36 shows the concentrations of nitrogen in the films. Looking away from the 3 sccm film, the concentration increases with N₂-flow, as expected.

Although the concentration generally increases with nitrogen flow for the rest of the samples this is not the case for the bottom part of the 2 sccm and 5 sccm films. For the 2 sccm film the concentration is $\sim 6 * 10^{20} \text{ cm}^{-3}$ at the surface. Then it decrease to $\sim 6 * 10^{20} \text{ cm}^{-3}$ at the depth of 100-150nm before it start to increase with depth until the concentration of $\sim 1 * 10^{21} \text{ cm}^{-3}$ is reached at the interface between the film and substrate. Because of this the concentration extends that of the 5 sccm sample in it's bottom $\sim 150 \text{ nm}$ and also in a thin part of it's top region. Similarly the nitrogen concentration at the bottom $\sim 225 \text{ nm}$ of the 5 sccm sample extends that of the 7 sccm film.

The reference sample has a nitrogen concentration of about 10^{19} cm^{-3} , although it was created with zero nitrogen flow. After a depth of about 400 nm the concentration increase steadily with depth eventually reaching 10^{21} cm^{-3} at the bottom of the film. This is a concentration in the same range as that for the film with highest nitrogen flow during deposition.

The 3 sccm sample stands out from the trend with a nitrogen concentration above that of the 10 sccm sample. At the bottom of the film the nitrogen content reaches the same value as that for the 20 sccm sample.

5.3 Heat treated films

5.3.1 Hall

Figure 16, and 18 show the carrier concentration, mobility and resistivity as measured by Hall for the heat treated films.

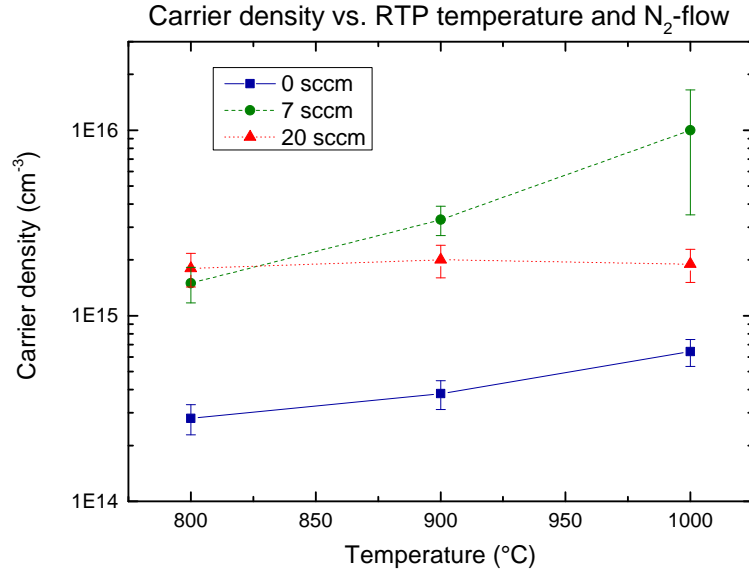


Figure 16: Carrier density versus heat treatment temperature.

In Figure 16, showing the carrier density of the heat treated films, it can be seen that the density generally increase with temperature, although for the 20 sccm film the concentration has a slight decrease from 900°C to 1000°C. For this film the variation is also much smaller than for the other samples. When comparing the carrier densities with those for the as-deposited films in Figure 9, however, it is clear that carrier density has substantially decreased after heat treatment.

For the 0 sccm film the carrier concentration is in the order of 10^{14} , as opposed to 1.7×10^{15} for the as-deposited film. The 7 sccm sample has a carrier density in the order of 10^{15} and 10^{16} after heat treatment, while the as-deposited sample has a density of about 4×10^{17} . In the 20 sccm sample, the carrier density is in the order of 10^{15} , as opposed to about 6.7×10^{18} for the as-deposited sample.

The decrease in carrier concentration after heat treatment is probably a result of nitrogen leaving the samples at the temperatures used, which can be explained by an increase in its diffusivity. Although the carrier density is lower for all samples compared to the as-deposited ones, an increase with RTP

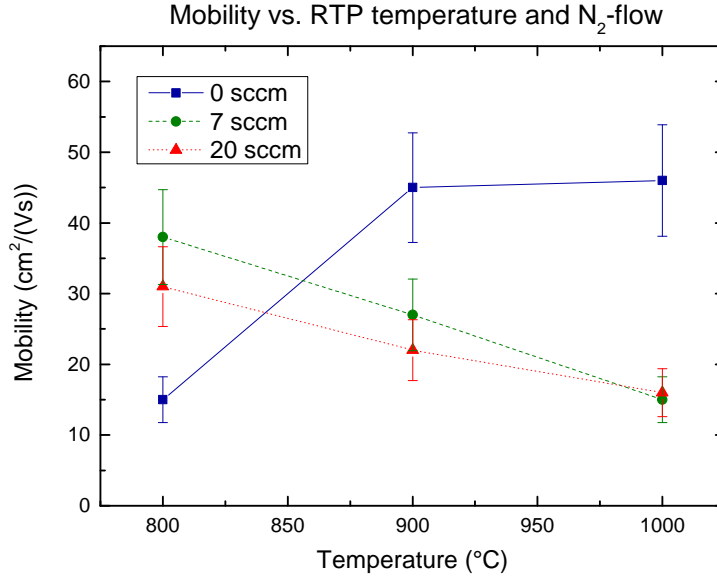


Figure 17: Mobility versus heat treatment temperature.

temperature is seen. This is probably due to intrinsic effects, for instance an increase in copper vacancies with RTP temperature.

0 sccm: The increase in carrier density is about $1 * 10^{14}$ from the 800°C to the 900°C film and $2.6 * 10^{14}$ from the 900°C to the 1000°C film.

7 sccm: The increase is higher with temperature than for the other N₂-flows, being in the order of 10^{15} .

20 sccm: The increase is about $2 * 10^{14}$ from the 800°C to the 900°C film, and the decrease from the 900°C to the 1000°C film is about $1 * 10^{14}$.

In Figure 17 the mobility versus RTP temperature is shown. Compared to the as-deposited values, the mobility has increased substantially for all heat treated samples, which is another indication that nitrogen is gone. For the 0 sccm films the mobility increases with RTP temperature. This is probably due to increased grain sizes with temperature, resulting in less grain boundaries. However, the increase from the 900°C film to the 1000°C film is only $1\text{cm}^2/(\text{Vs})$.

For the 7 sccm and 20 sccm samples the mobility decrease with temperature. In other words the heat treatment has had a different effect on these films than on the reference film. As seen from the SEM measurement more pinholes are created when the RTP temperature increase, and the number and sizes of these are larger the higher the N₂-flow. Maybe these are causing the mobility to decrease.

In Figure 18 the resistivity for the heat treated films is shown versus temperature. For the 0 sccm and 7 sccm films a decrease with temperature occur.

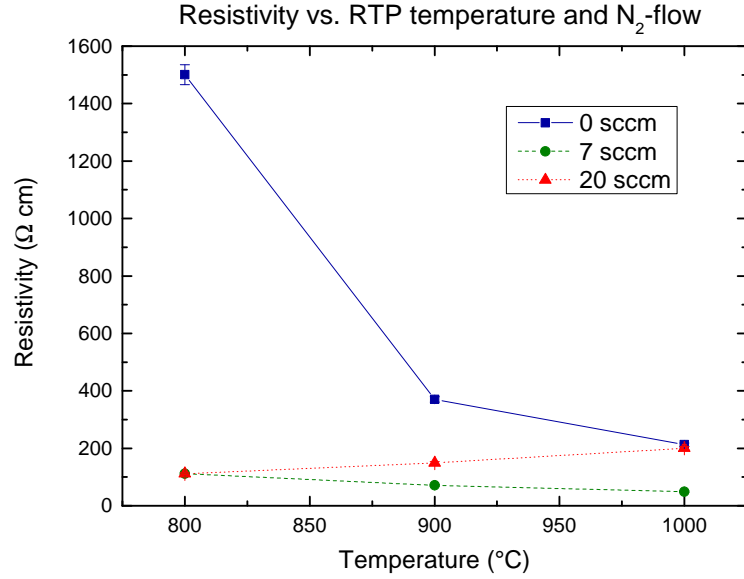


Figure 18: Resistivity versus heat treatment temperature.

On the other hand, for the 20 sccm sample the resistivity increase with temperature. Resistivity is inversely proportional to both carrier density and mobility. In the 0 sccm film both of these quantities increase with RTP temperature, and so the decrease in resistivity is as expected. In the 7 sccm and 20 sccm sample, however, the carrier concentration increase with temperature, while the mobility decrease. For the 7 sccm film this causes the resistivity to decrease with temperature, while for the 20 sccm film, it increases with temperature. The increase in resistivity with temperature for the 20 sccm sample is as expected, since the variation in carrier concentration with temperature is small, and the mobility decrease with temperature.

5.3.2 Temperature dependent Hall

For the Cu_2O films which were heat treated at 900°C , temperature dependent Hall (TdH) was measured at temperatures ranging from 120 K to 2129 K. In this measurement the temperature was not high enough to determine $N_a - N_d$, which mean that N_d and N_a could not be determined separately, only the N_d/N_a ratio. Also, the acceptor energy level relative to the valence band edge, E_a , was determined.

The results can be seen in Table 2 and Figure 19 and 20

N-flow (sccm)	N_d/N_a	Std. error N_d/N_a	E_a (eV)	Std. error E_a (eV)
0	0.77721	0.00821	0.20599	9.12695 E-4
7	0.75923	0.01097	0.16266	0.00116
20	0.61453	0.04293	0.20879	0.00304

Table 2: Ratio of donor to acceptor concentration, N_d/N_a , and acceptor energy level, E_a , for the samples that were heat treated at 900°C .

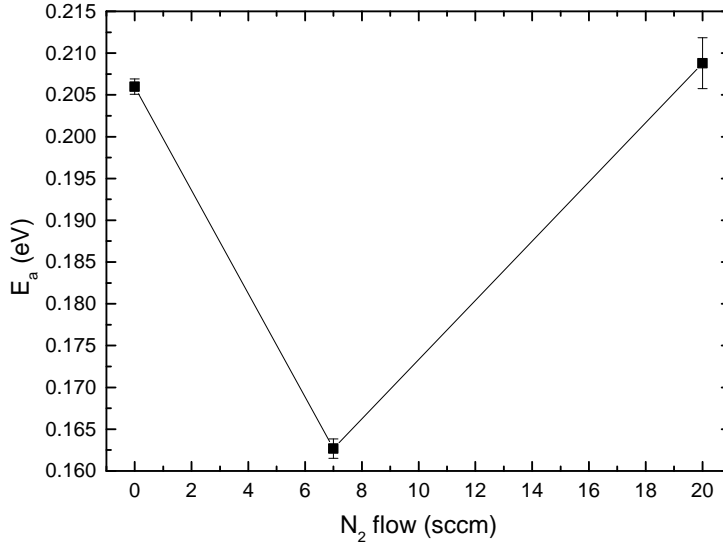


Figure 19: Acceptor energy level, E_a , for different N_2 -flows of 900°C heated samples.

The ratio of donor to acceptor concentration, N_d/N_a , has a value ranging from about 0.61 to 0.78. This indicates that donors are present in the Cu_2O films at concentrations between about 60 and 80 % of the acceptor concentration. As one would expect, the ratio of donors are lower, the higher the N-flow.

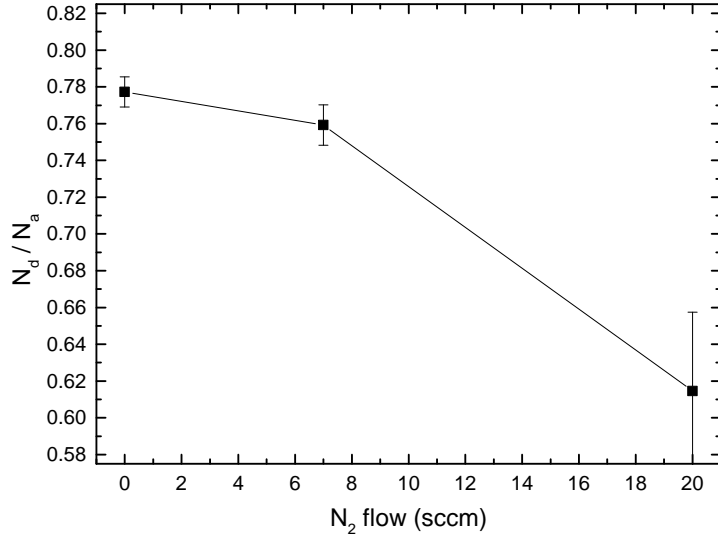


Figure 20: Ratio N_d/N_a for different N_2 -flows of 900 °C heated samples.

The acceptor energy level is different for all three samples. The 7 sccm value is most clearly different from the other samples. For the 0 sccm and 20 sccm film the acceptor levels are equal within 0.01 eV, while for the 7 sccm film it is about 0.4 eV below these values. This indicates that holes are provided by a different impurity in the 7 sccm film from the 0 sccm and 20 sccm films. The impurities might also be different for the 0 sccm and 20 sccm samples, but the difference is small enough to be accounted for by the standard error of the 20 sccm sample.

5.3.3 XRD

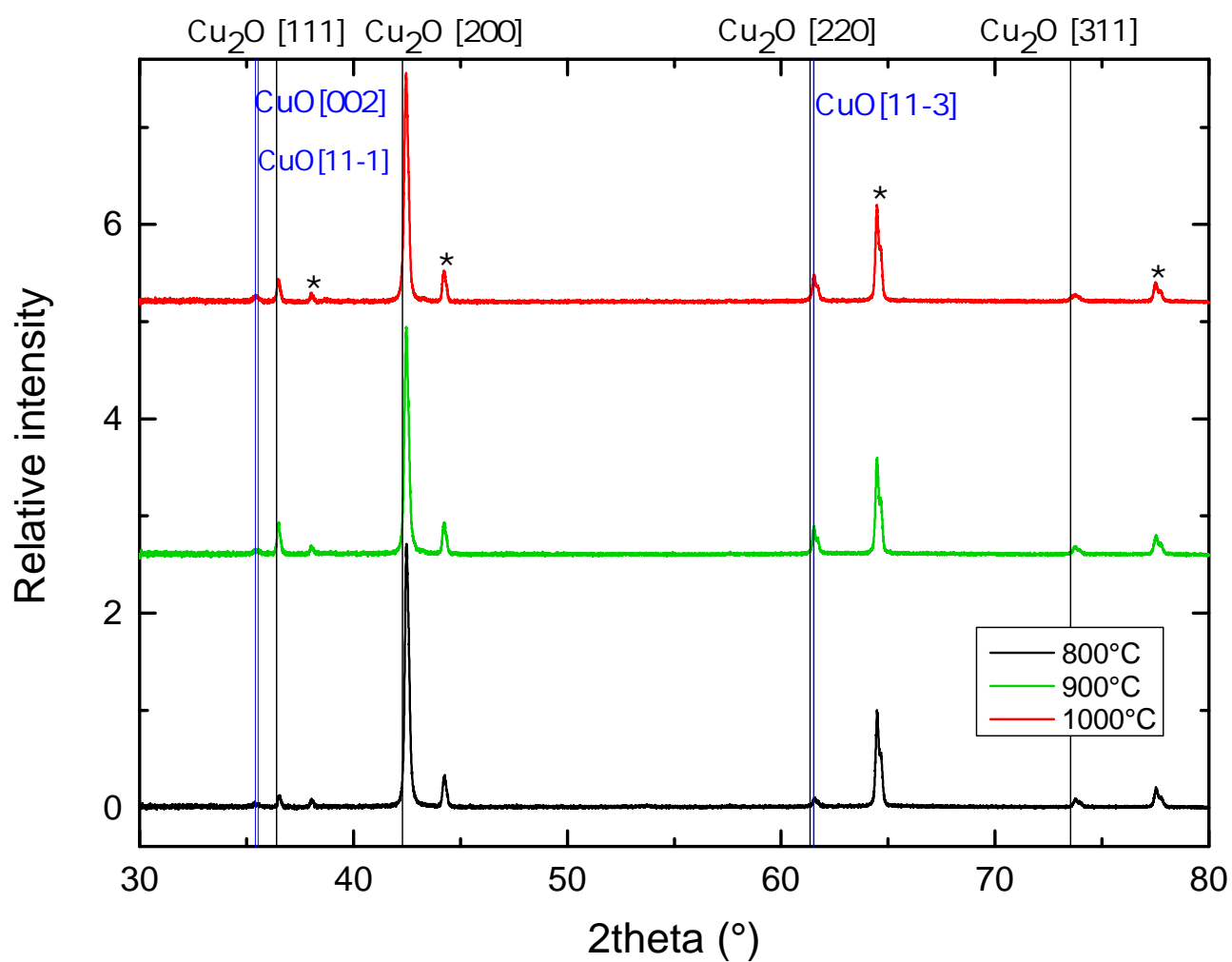


Figure 21: XRD plots of heat treated 0 sccm samples. Bottom graph: 800°C, middle: 900°C, upper: 1000°C. Background peaks are indicated with an asterisk (*).

As for the as-deposited films, XRD measurements of the heat treated samples were done with 2θ angle ranging from 30° to 80°, and the patterns were

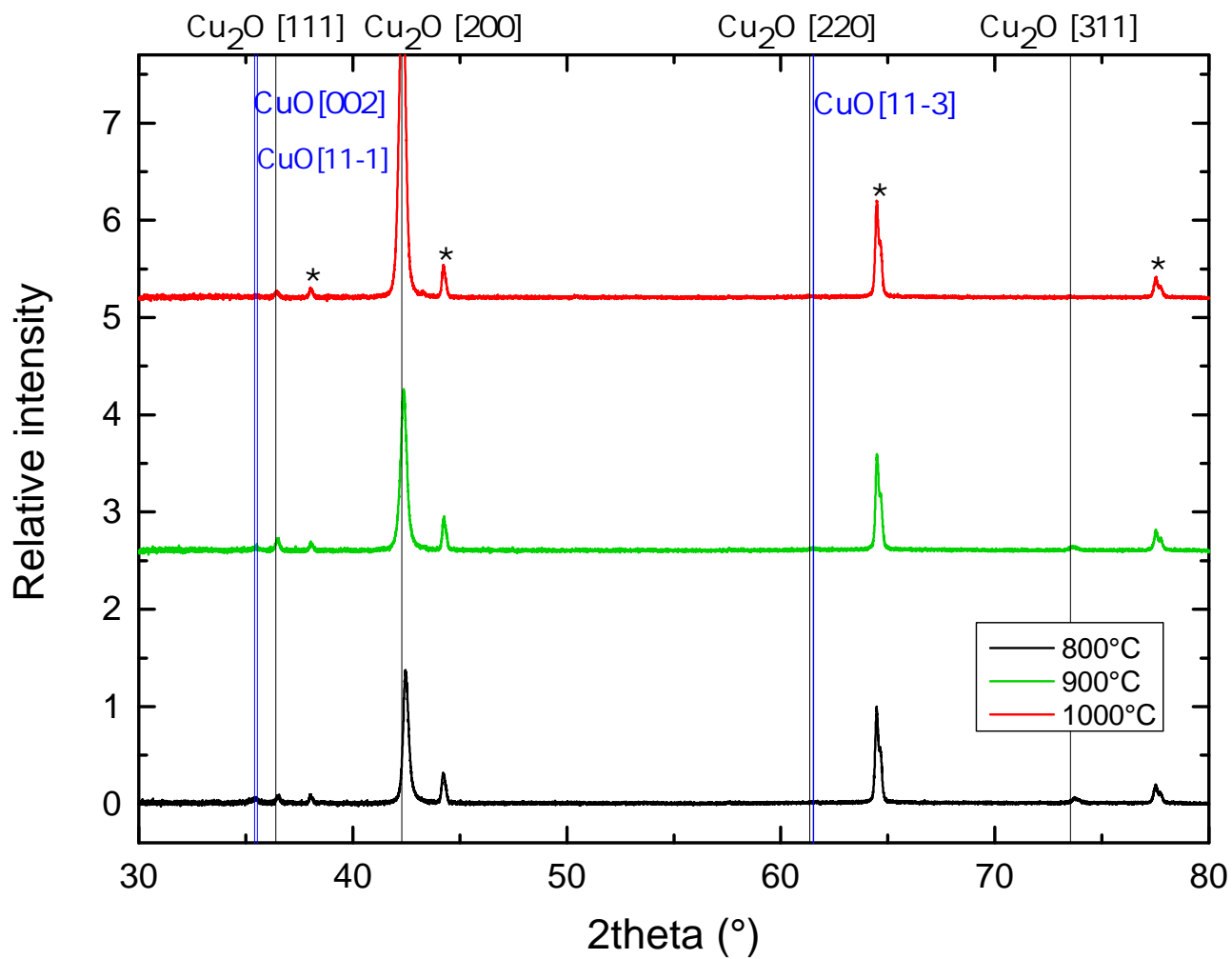


Figure 22: XRD plots of heat treated 7 sccm samples. Bottom graph: 800°C, middle: 900°C, upper: 1000°C. Background peaks are indicated with an asterisk (*).

compared with reference spectra of cuprous oxide, cupric oxide and metallic copper, as well as substances containing both copper and nitrogen. As for the as-deposited films, neither pure copper or combinations of copper and nitrogen were seen in any of the films. In order to allow comparison of intensities among

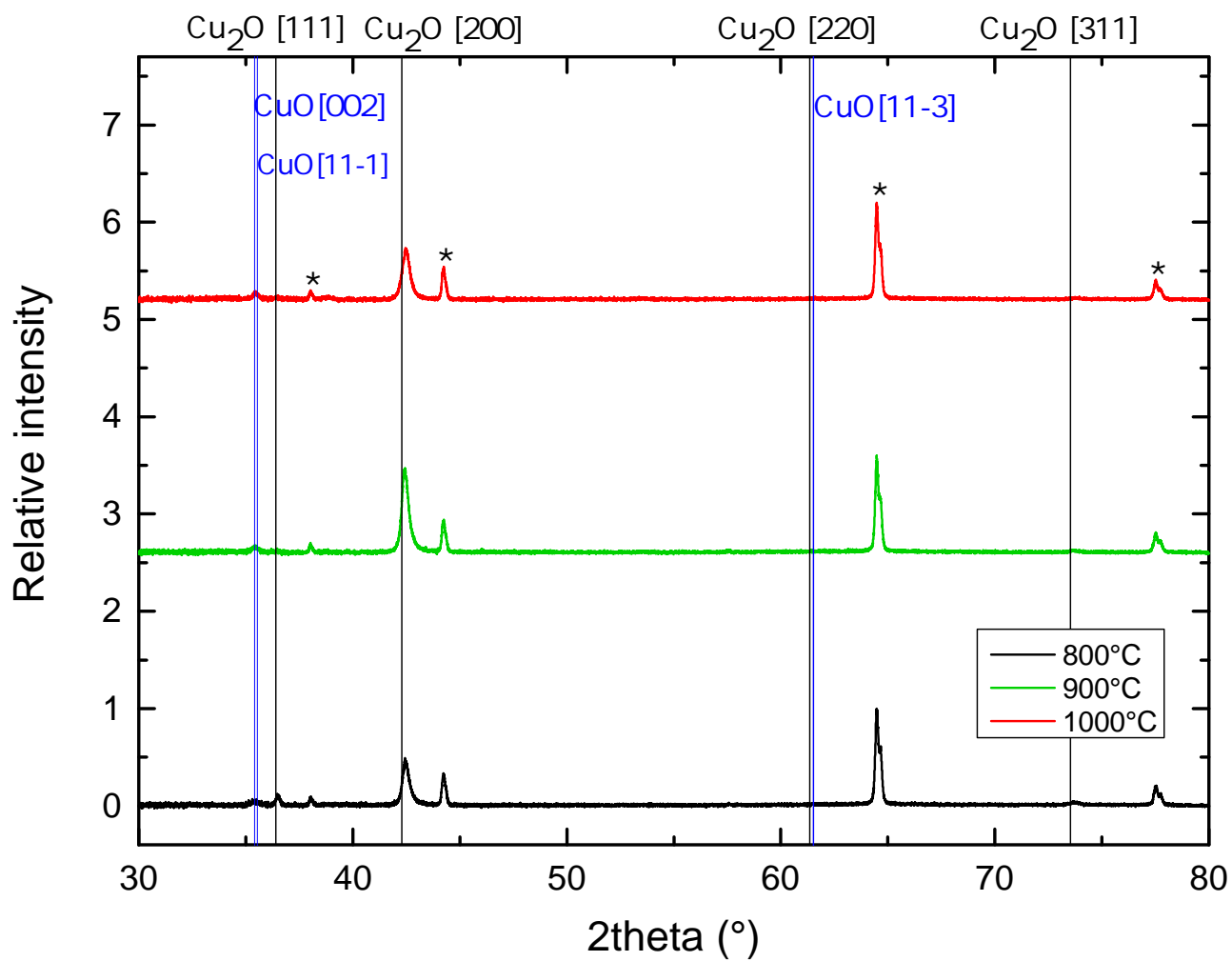


Figure 23: XRD plots of heat treated 20 sccm samples. Bottom graph: 800°C, middle: 900°C, upper: 1000°C. Background peaks are indicated with an asterisk (*).

samples having the same N-flow, intensity spectra for each N-flow were normalized. This was performed after the background peak from the sample holder at $2\theta = 65.4^\circ$, so that intensities of the spectra are given in units of this peak's intensity.

Figure 21, 22 and 23 shows the XRD plots of the heat treated films with 0 sccm, 7 sccm and 20 sccm nitrogen flow, respectively. Positions of known Cu_2O and CuO peaks from powder samples are marked with vertical black and blue lines, respectively. Sample holder peaks are marked with an asterisk(*).

For all the samples, the peaks are somewhat to the right of the reference lines, which could be a sign of smaller lattice distances in the films deposited. This is common for thin films compared to powder samples. However, it could also be due to instrumental factors, and care should be taken in interpreting their absolute values. It is more informative to look at how the 2θ positions change for different temperatures and N-flows.

For the 0 sccm films, at all temperatures, four intensity peaks of Cu_2O structure can be seen in Figure 21. These correspond to (111), (200), (220) and (311) orientation. The Cu_2O (200) peak is by far the most prominent. The others Cu_2O peaks are quite small, where the Cu_2O (311) peak is the smallest. In addition to Cu_2O peaks, a barely visible intensity peak, corresponding to CuO structure can be seen for all temperatures, although for the one at 800°C it is almost invisible. This peak fits with two orientations: CuO (002), at $2\theta = 35.4$, and CuO (11 - 1) at $2\theta = 35.5^\circ$. Also, it could be speculated if the Cu_2O (220) peak have some contribution from (11 - 3) oriented CuO . Thus, at most three CuO peaks are represented, however with very low intensities.

For the 7 sccm samples the XRD spectra are showed in Figure 22. The Cu_2O visible peaks are the same as for the 0 sccm samples with one exception: The peak corresponding to both Cu_2O (220) and CuO (11 - 3)), at $2\theta = 61.3^\circ$ is invisible for the 800 and 1000°C samples, while being almost invisible for the 900°C sample. For the 1000°C sample, the Cu_2O (311) peak at $2\theta = 73.5^\circ$ is also gone.

For the 7 sccm sample at 1000°C , the pure CuO peak at about $2\theta = 35.4^\circ$ is also gone.

Figure 23 show sthe XRD plots for the 20 sccm samples. Now even more Cu_2O peaks are gone or reduced compared to the spectras of the 0 sccm samples compared to the 7 sccm spectra. The peak corresponding to both Cu_2O (220) peak and CuO (11 - 3), at $2\theta = 61.3^\circ$, is gone for all samples. In addition, the Cu_2O (111) peak at $2\theta = 36.4$ is only visible for the 800°C sample. The Cu_2O (311) peak at about $2\theta = 73.5^\circ$, is almost invisible for all temperatures, being only a suggestion in the plott of the 1000°C sample. The only clear Cu_2O peak for the 20 sccm samples is the Cu_2O (200) peak, however, this has only about half the intensity in the 20 sccm spectras than in those for the 0 sccm and 7 sccm samples, suggesting less Cu_2O structure in the 20 sccm films than in the 0 sccm and 7 sccm heat treated films.

Figure 28 shows the how the intensity of the Cu_2O (200) peak varies with temperature for the 0 sccm, 7 sccm and 20 sccm films. However, the intensity does not seem to have any dependence on the RTP temperature. It decrease with N-flow if one looks away from the value of the 7 sccm 1000°C peak. However, this can be explained by the decrease in film thickness with temperature.

The Cu_2O [200] and [311] peaks seem to have same intensity value for all temperatures, while this is not the case for the Cu_2O [111] and [220] peaks. The Cu_2O [111] peak have the highest intensity for the 900°C sample and the lowest for the one at 1000°C . The peak at about $2\theta = 61.3$, corresponding to Cu_2O [220], and maybe CuO [11 – 3], orientation, has about the same intensity for the films heated at 800°C and 900°C , but decreases for the sample at 1000°C . This could mean that the overall Cu_2O intensity decrease for the sample heated at 1000°C , compared to the other two, as long as none of the peaks get wider instead.

Some small changes in the FWHM value and position of the peaks occur with temperature, all in the order 0.01° :

Figure 24 shows the variation in FWHM value of the Cu_2O (200) peak for all samples. It increase with temperature for both the 7 sccm and 20 sccm sample, which might correspond to a decrease in grain size. For the 0 sccm sample, it also increases from 800 to 900°C , but then remains the same as for the 900°C sample in the sample at 1000°C .

The position of the Cu_2O (200) peak, as shown in Figure 25, decrease with temperature for the 0 sccm and 7 sccm sample, which according to Bragg's law corresponds to a larger distance between these planes with temperature. For the 20 sccm sample the position decrease from 800°C to 900°C , but then increases for the 1000°C sample, having the highest value. In other words the lattice distance of the Cu_2O (200) direction is smaller for the 20 sccm sample when heated at 1000°C compared to the lower temperatures.

Figure 26 shows the FWHM value of the peak that represents the Cu_2O (111)-direction for the 0 sccm and 7 sccm sample respectively. The FWHM of the Cu_2O (111) peak increase with temperature for the 0 sccm and 7 sccm sample. The 20 sccm sample was not measured, because the peak was not visible for all temperatures.

The position of the Cu_2O (111) peak, as shown in Figure 27, does not have a trend. For the 0 sccm sample it first decreases from 800°C to 900°C . Then it increases to a value in between the first two for the 1000°C sample. The 7 sccm sample, on the other hand, has an increase in the position from 800°C to 900°C , and then a decrease to the lowest value for the 1000°C sample.

The FWHM value and position of the Cu_2O (311) peak was only measured for the 0 sccm sample. As for the other peaks, the FWHM increase with temperature. The position, however has no clear trend, first decreasing from 800 to 900°C , and then increasing from 900 to 1000°C .

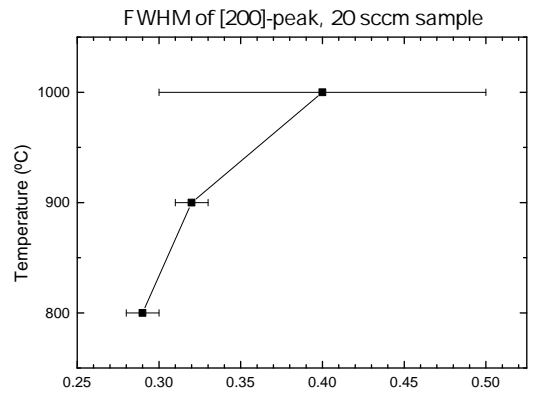
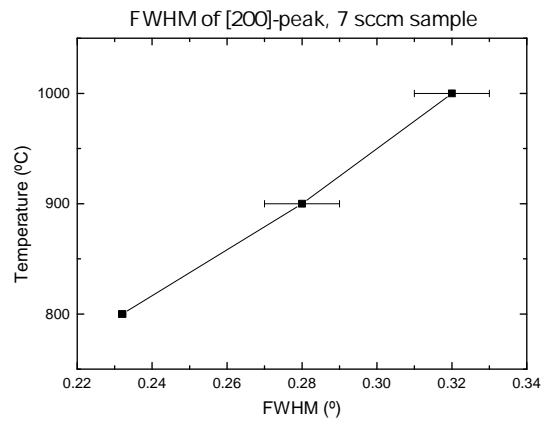
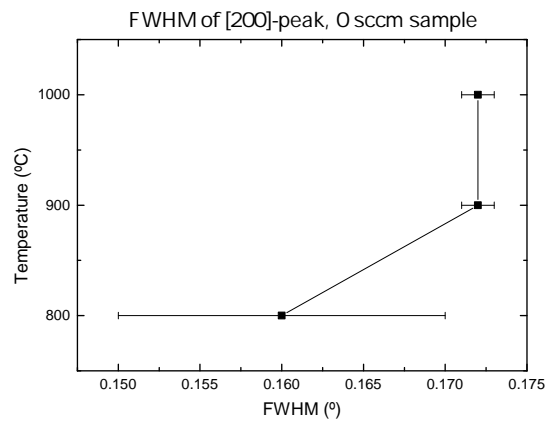


Figure 24: Full Width Half Maximum of the Cu_2O (200) peak versus RTP temperature for the 0 sccm, 7 sccm and 20 sccm samples.

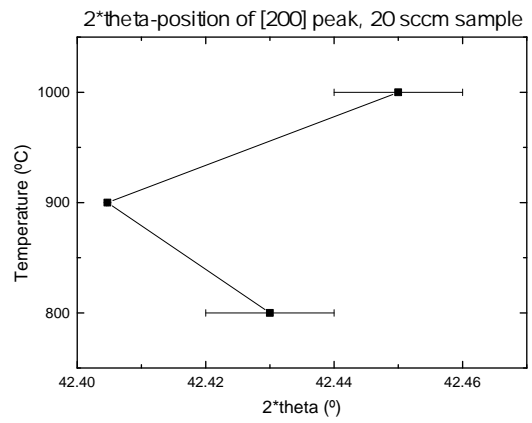
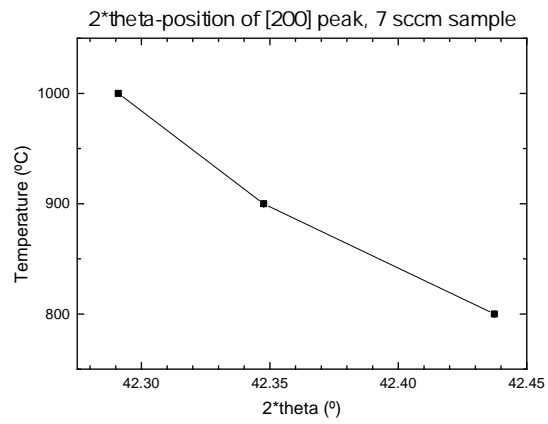
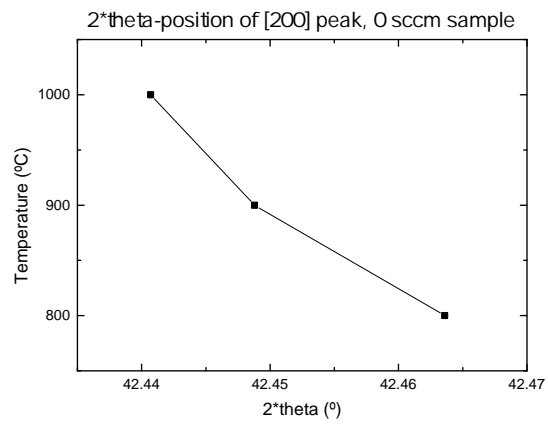


Figure 25: Variation of 2θ position of Cu_2O (200) peak with temperature for the 0 sccm, 7 sccm and 20 sccm samples.

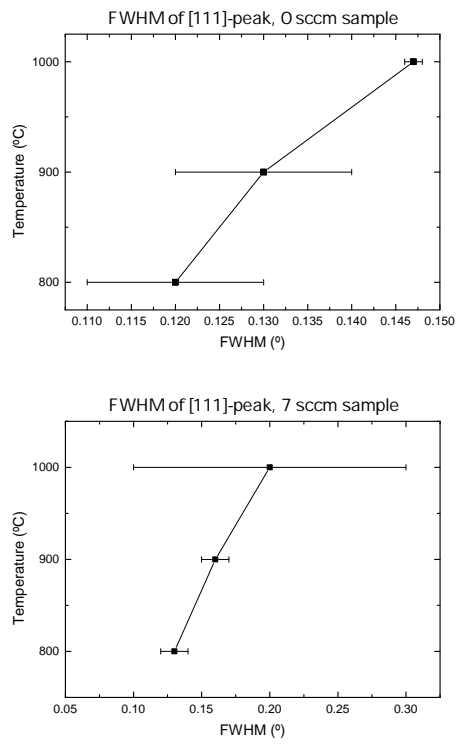


Figure 26: Full Width Half Maximum of the Cu_2O (111) peak as a function of temperature for the 0 sccm and 7 sccm films.

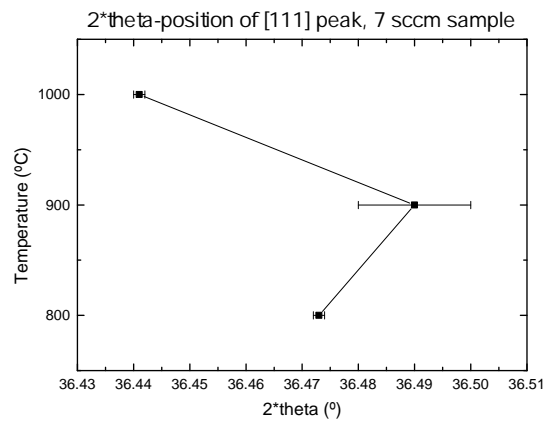
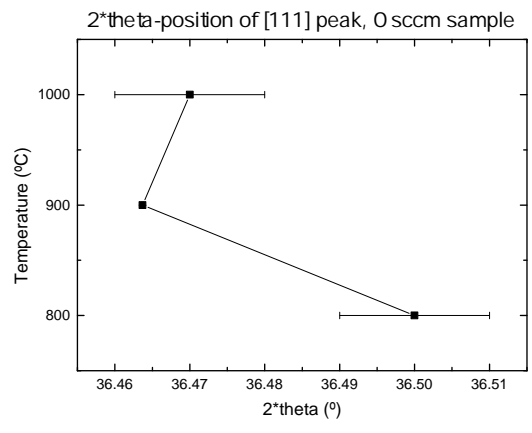


Figure 27: Variation of 2θ position of Cu_2O (111) peak with temperature for the 0 sccm and 7 sccm samples.

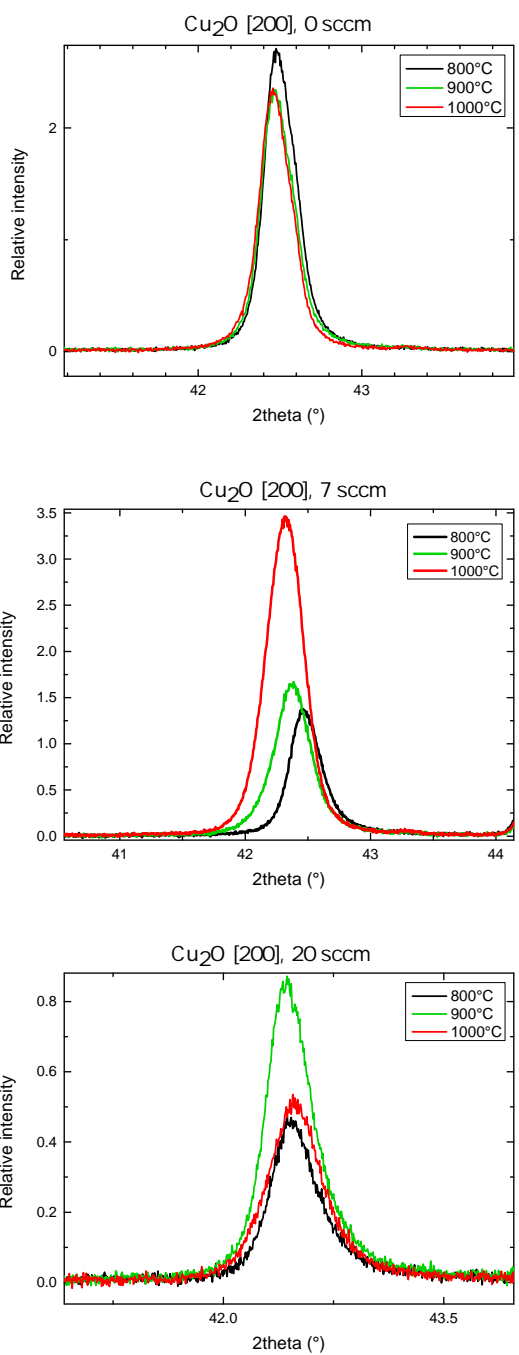


Figure 28: Intensity variation of the Cu_2O (200) peak with temperature for the 0 sccm, 7 sccm and 20 sccm heat treated samples.

5.3.4 UV-vis

Figure 29 shows transmittance measurements of the heat treated samples. Just

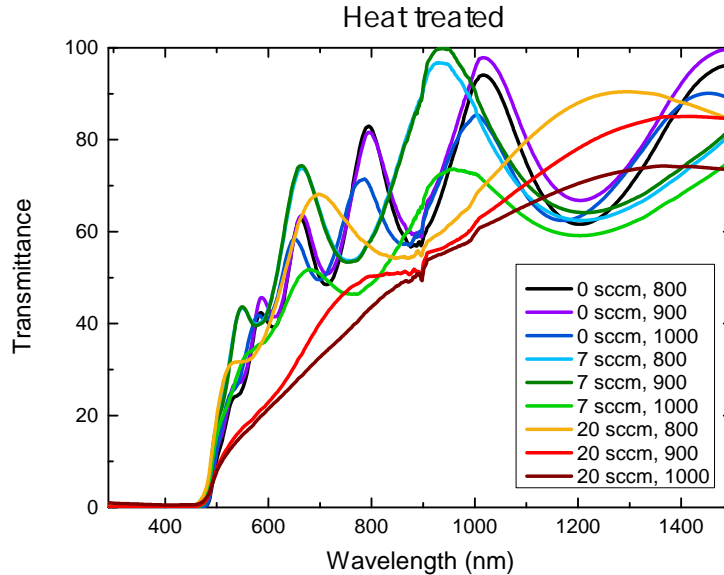


Figure 29: Transmittance measurements of heat treated samples.

as for the non heated samples in Figure 13 there is almost zero transmittance in the wavelength range of 290 nm to about 470 nm. These wavelengths corresponds to the ultraviolet and blue part of the spectrum. Then the transmittance increases substantially for higher wavelengths.

The transmittance of the reference sample seems to slightly increase for the 900°C sample compared to the 800°C sample. For the 1000 °C reference sample, however, the transmittance is clearly lower than for both the 800°C and 900°C sample. All three samples have the same amount of Kiessig fringes, about five or six. However, unlike the 800°C and 900°C samples, which have the same distance between the fringes, the 1000°C film has a slightly shorter distance, indicating a thicker film.

Also for the 7 sccm sample, the transmittance is higher for the 900°C sample than the 800°C sample, while the 1000 °C sample has a clearly lower transmittance than the two other films for all wavelengths. Also, the Kiessig fringes are quite correlated between the 800°C and the 900°C sample, while they are slightly moved to the right for the 1000°C film, indicating that this is thinner than the two others.

For the 20 sccm samples the trend is different than for the 0 sccm and 7 sccm samples. Both the 900° and 1000° sample has a significantly lower transmittance

than the both the 800°C film and the other heat treated films in the wavelength interval of about 500 nm to 1000nm, where they increase almost linearly with wavelength, reaching a value of 60–70% at the end. On the other hand, the transmittance of the rest of the heat treated films first increases almost linearly in the beginning of this interval, while then gradually reaching a plateau value, of which the transmittance varies. This plateau value is around 60% or 70%.

Also, the 20 sccm films heated at 900°C and 1000°C have no Kiessig fringes, like the rest of the films, which could indicate a difference in the surface structure. This is as observed in the picture of the films, as shown in Figure 8, where it can be seen that the 20 sccm films at 900°C and 1000°C has a slightly greyish or whitish colour. This is also seen in the 7 sccm sample at 1000°C, which also has a lower transmittance than the rest of the films. However, this film has Kiessig fringes.

From the figure it is also seen that the 20 sccm sample that was heated at 1000 °C is the only sample with a transmittance above zero in the visible wavelength interval between 290 nm and about 460 nm. This is probably due to a hole in the film, which could not be avoided in the opening of the light beam. Because of this the transmission value might be somewhat higher than it should have been for all wavelengths measured, although as seen from the first interval, it is at most higher by a couple of percent.

5.3.5 SIMS

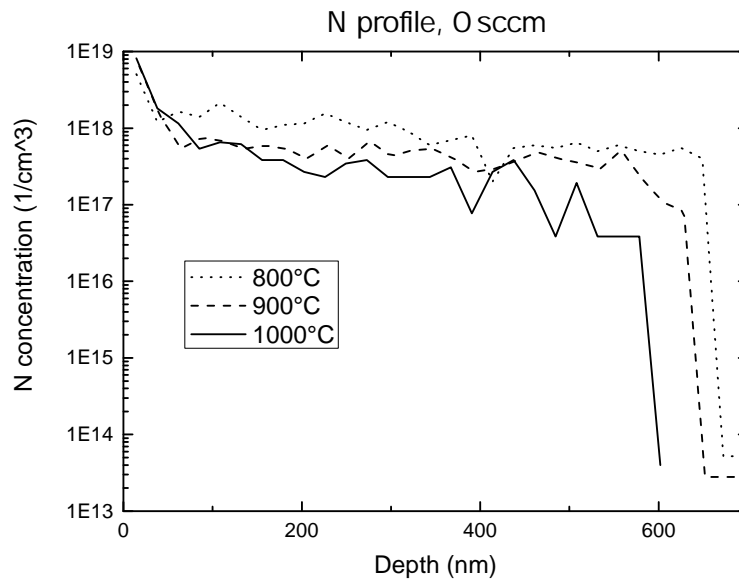


Figure 30: N profile for 0 sccm heat treated sample.

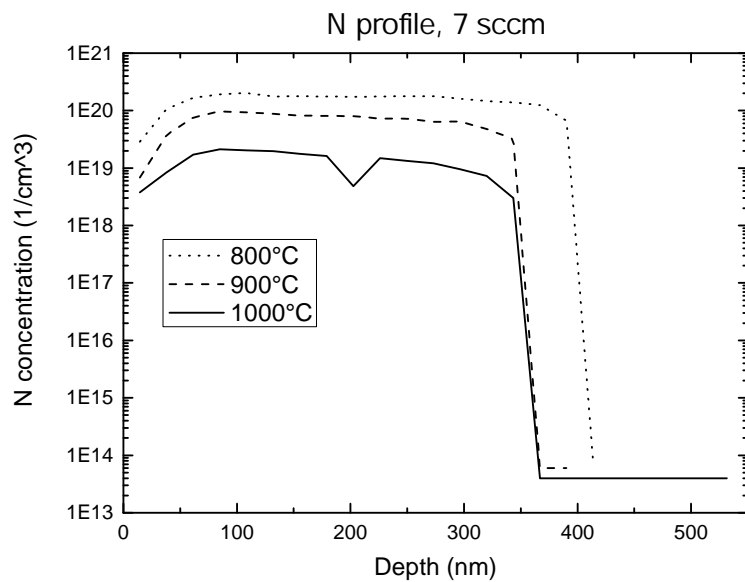


Figure 31: N profile for 7 sccm heat treated sample.

In order to estimate the nitrogen concentration in the heat treated films, SIMS measurement was conducted.

Figure 30, 31 and 32 shows the nitrogen depth profile for the 0 sccm, 7 sccm and 20 sccm samples, respectively. One can see that the concentration decreases with RTP temperature for all samples. This confirms that nitrogen leaves the samples during RTP.

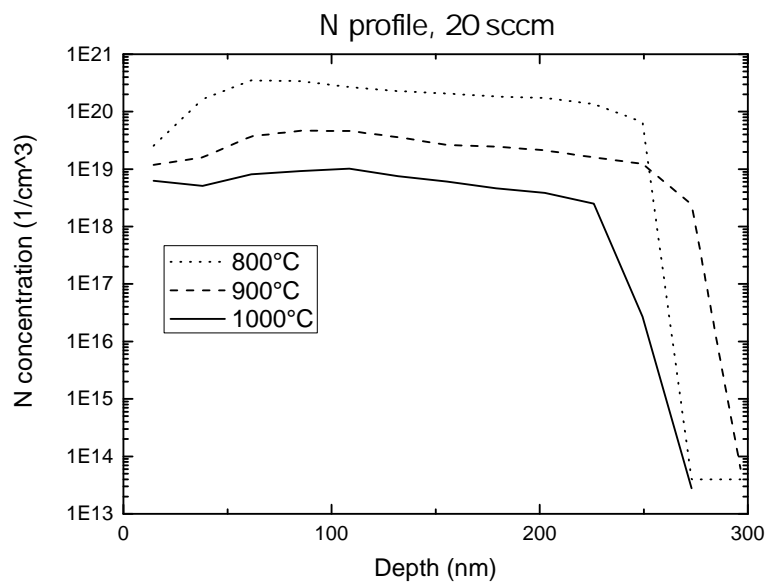


Figure 32: N profile for 20 sccm heat treated sample.

5.3.6 SEM

Images of the 0, 7 and 20 sccm heat treated samples can be seen in Figure 33, 34 and 35, respectively.

Some white looking spots, or lumps, can be seen on the SEM images. These indicate particles lying on top of the surface, i. e. above the rest of the film. The white color result from a charging effect during measurement, which result for low conductivity films. For the 20 sccm films, white looking spots were covering the whole film. However, for the 20 sccm film heated at 1000°C, they were not as white compared to the rest of the surface, which indicate that are merged into the film.

For the 0 sccm and 7 sccm samples at all temperatures the white looking particles on top of the surface were only a few, not covering the whole film. This was also the case for the as-deposited films.

The images shows that the grain size increase with temperature for all samples, as expected. Also, a large amount of holes, so called pin holes, occur in the films after heat treatment, especially for the films with nonzero N₂-flow at 900°C and 1000°C. Maybe this is a result of vacancies in the films that diffuses to make bigger holes during heat treatment. If so, the number of vacancies might be larger in the films with a high N₂-flow due to the escape of nitrogen from the sample.

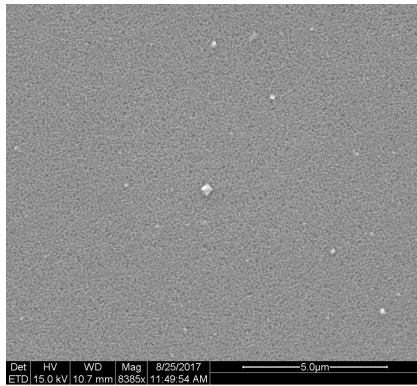
In the following are some detailed observations of each film:

0 sccm, as-deposited:

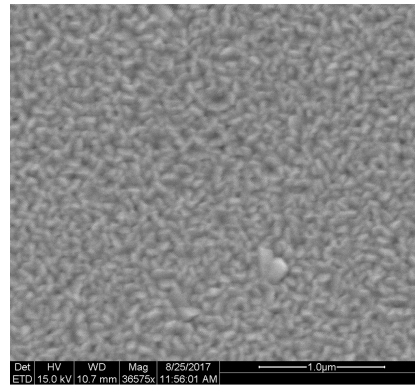
Typical grain length: 0.08μm to 0.25μm. However, as seen from the picture zoomed in, two grains right beside each other is larger, having lengths in the order of the largest grains and widths twice or three times as large. This couple of grains seem to be at a higher level than the surface level, as it has a lighter color. There also is one similarly sized grain, which seems to immersed into the surface. On the first picture of the 0 sccm as-deposited sample white spots can be seen. The biggest is about 0.36 * 0.36μm², while the smallest are about 0.16*0.07μm². The grains have rounded cylindrical shapes, a bit like rice grains or pills. But maybe they would look more irregular if the resolution was better. There seem to be some holes or cracks between grains, but maybe they are just pit-holes. They are small compared to the grains, and not as clear and circular as the pinholes seen in samples heated at higher temperatures, probably due to their small sizes.

0 sccm, 800°C:

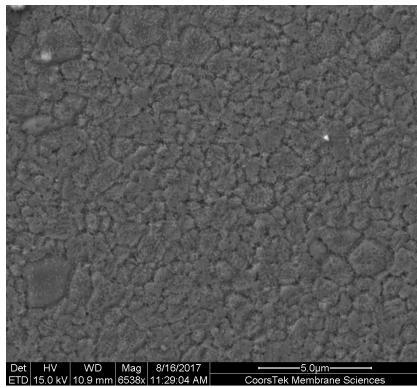
The grains are irregularly shaped, not like rounded cylinders, as for the as-deposited sample. Grain size vary a lot: From less than 0.5μm to about 2.7μm. Many of the grains are covered with small dark spots. When zooming in, these spots seem to be clearly defined with roughly shaped edges. There appear three brighter spots on the picture. The whitest and clearest is comparable in size with the smallest grains, being 0.33μm at its widest. The other two appear less bright and more smeared out than the first. They are about 0.5 and 0.75μm at



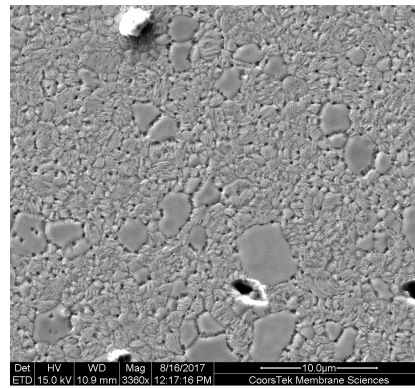
(a) as-deposited



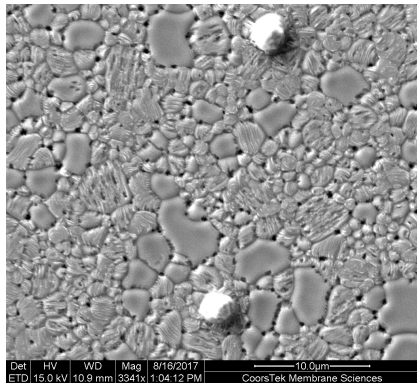
(b) as-deposited



(c) 800°C

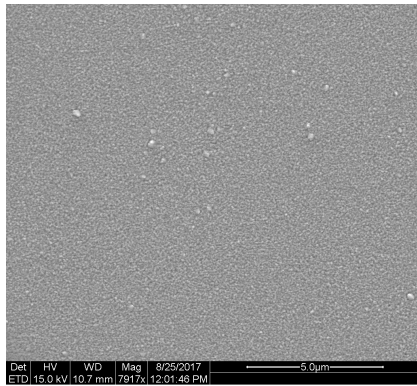


(d) 900°C

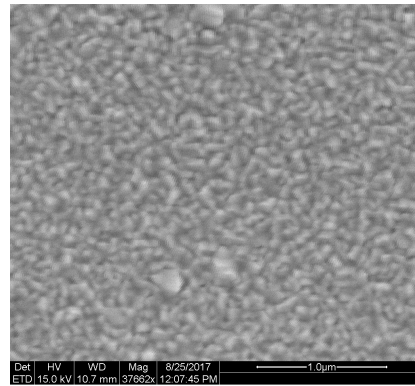


(e) 1000°C

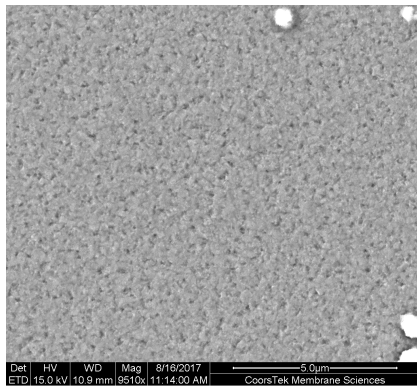
Figure 33: SEM images of as-deposited and heat treated films of 0 sccm nitrogen flow.



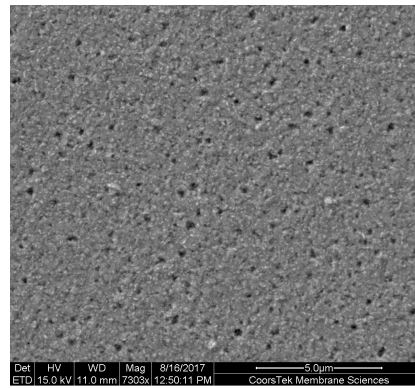
(a) as-deposited



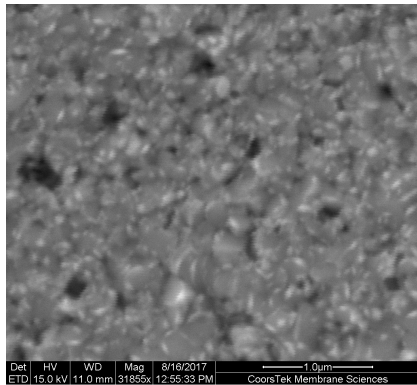
(b) as-deposited



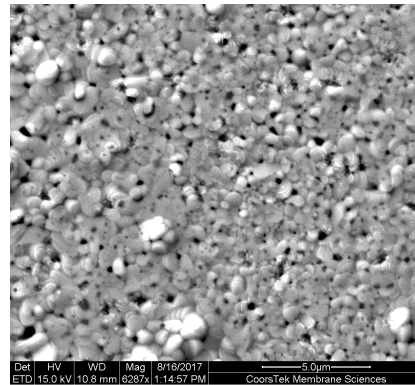
(c) 800°C



(d) 900°C

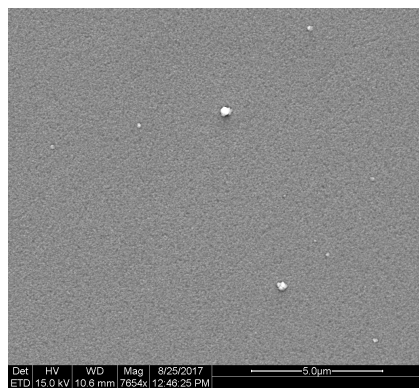


(e) 900°C

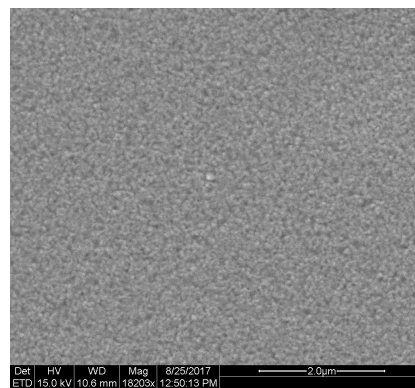


(f) 1000°C

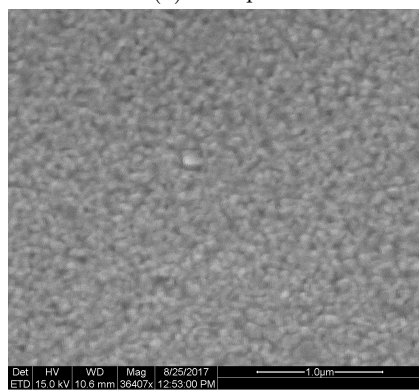
Figure 34: SEM images of as-deposited and heat treated films of 7 sccm nitrogen flow.



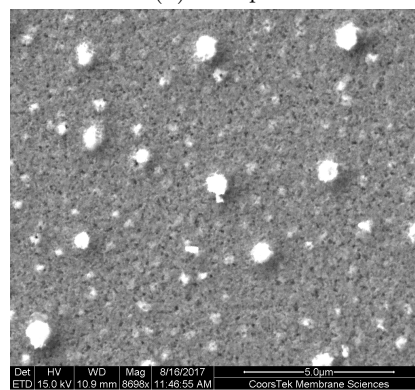
(a) as-deposited



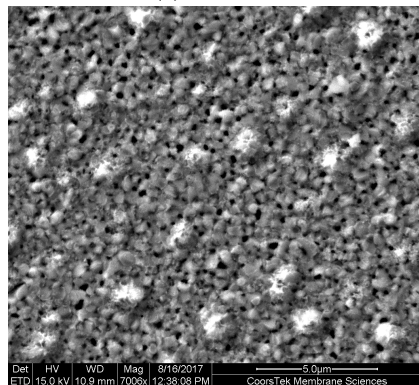
(b) as-deposited



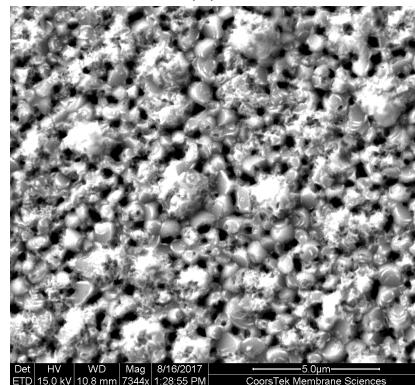
(c) as-deposited



(d) 800°C



(e) 900°C



(f) 1000°C

Figure 35: SEM images of as-deposited and heat treated films of 20 sccm nitrogen flow.

their widest. Some cracks and pinholes are seen at the grain boundaries. These are about a fifth in size of the smallest grains at their biggest.

0 sccm, 900°C:

One can clearly see two types of grains: Some have completely smooth surfaces, while others have irregular stripes on their surfaces, which may be edges of layers constituting these grains. The grains are irregularly shaped, not like rounded cylinders, as for the as-deposited sample.

The grains are larger than for the 800°C film. Lengths of rough grains: From about 0.5 μm to 3.3 μm . Lengths of smooth grains: From about 0.8 μm to 5.5 μm .

A white lump, probably what was seen as a white spot in the lower temperature films, can be seen. It clearly seems to be lying on top of the rest of the surface and has a size of about 2 * 3 μm^2 .

As opposed to the as-deposited and 800°C films, one can now clearly observe many small pinholes, about 0.1 – 0.2 μm in size. These are both located on and around the the grains. In addition, a few much larger pinholes are seen. The biggest, seems to have comparable size as the white lump, of about 2–3 μm . These big pinholes seemed to be representative for the whole film, not only at the area shown in the picture.

0 sccm, 1000°C:

As in the film heated at 900°C, there are two types of grains: Some are rough, and some are smooth. The smooth grains are generally larger, but some of the rough grains are comparable in size.

Lengths of rough grains: From about 0.5 μm to 4.8 μm . Lengths of smooth grains: From about 1 μm to 6.5 μm .

The biggest white lump now has a length of 3.6 μm . This is an increase in size compared to the biggest of the 800°C sample, having a lump of 0.3–0.75 μm , and the 900°C sample of 3 μm .

Pinholes are clearly seen, as for the 900°C film. However, huge pinholes are not seen, as for the 800°C film, only holes of sizes up to about 0.7 μm . The pinholes are mostly located on the grain boundaries. Some of the rough grains have holes on them, but generally these are more like dents, or dents with one or two small holes within.

7 sccm, as-deposited:

Typical grain sizes: From 0.07 * 0.07 μm^2 to 0.07 * 0.19 μm^2 . Some bigger grains, embedded in the surface: Typically from 0.23 * 0.26 μm^2 to 0.27 * 0.35 μm^2 .

Some white grains, as seen on the most zoomed out picture, with similar sizes as the big, embedded grains.

As for the as-deposited film with 0 sccm of nitrogen there seem to be some holes or cracks between grains, but maybe they are just pit-holes. They are small compared to the grains, and do not appear as clear and circular as the pinholes seen in samples heated at higher temperatures, probably due to their small sizes.

The shapes of the grains seem to vary more than for the as-deposited 0 sccm

film. Some grains seem circular or oval, while others seem to be more irregular, although with rounded edges. The grain sizes of the as-deposited 0 sccm and 7 sccm films are about the same.

7 sccm, 800°C:

The grains seem to be rough and irregularly shaped. They are smaller, and so appear less defined, than for the 0 sccm sample at the same temperature. However, the grains are generally bigger than for the as-deposited sample: Typical grain sizes: The image is not very sharp, but grain sizes seem to be less than $0.5\mu\text{m}$ at widest, typically half that size, and maybe less.

A lot of pinholes are seen, more clearly defined than for the as-deposited sample. These are irregularly shaped and positioned at the grain boundaries. In general the pinholes are smaller than the grains, although some have the same length, or larger, than the smallest grains.

Some white particles are observed with lengths from about $0.3\mu\text{m}$ up to at least $0.8\mu\text{m}$, but not covering the whole surface.

7 sccm, 900°C:

Typical grain size: About $0.5\mu\text{m}$ or less, although they are hard to separate. When comparing the picture of this sample with that for the 800°C film, it looks as though the grains are slightly bigger in this film.

Some slightly lighter colored grains are seen. These have the same sizes as the other grains, seeming to be part of the surface.

The pinholes between the grains seem bigger than for the 800°C sample.

When zooming in on the picture, one can see that the grains generally have less edges than before. Instead, some cylindrical and rounded shapes are seen. Many of the grains have curved stripes, which might be evidence of coin-like layers constituting them, as more clearly observed in the 1000°C 7 sccm film.

7 sccm, 1000°C:

The grains appear clearer than for the lower temperatures. Their shapes are rounded, for instance ovals or rounded triangles. Some grains have rounded stripes, as if they are constituted of layers. Typical grain lengths: From about $0.2\mu\text{m}$ to about $0.9\mu\text{m}$. Some of the biggest grains appear white, which indicates a rough surface. Pinholes are clearly seen, having sizes around those of the smallest grains.

20 sccm, as-deposited: Some grains seem to have been quadratic or circular, while others seem oval or rectangular. Some of the oval grains seem to be bent, like a banana. Typical grain sizes: The picture is not very sharp, but typical lengths seem to vary from about $0.06\mu\text{m}$ to $0.22\mu\text{m}$. Widths for all grain shapes are typically around $0.07\mu\text{m}$. One bigger grain, partially embedded in the surface, partially at a higher level, is seen: $0.2 * 0.2\mu\text{m}^2$. There are some white grains: Sizes seem to range between $0.09 * 0.09\mu\text{m}^2$ and $0.37 * 0.46\mu\text{m}^2$. One of the biggest white particles seem to actually be a cluster of four smaller grains. There also seem to be areas without white particles. The film seem

to contain a large number of pinholes of the same size as the smallest grains, although they also may be dents.

20 sccm, 800°C: Small grains: Not very sharp resolution, but the grain size seems typically to be about $0.1\mu m$ across. This is comparable to the grains of the 7 sccm sample, heated at the same temperature. However, some grains are much larger, about 7 Pinholes at comparable size with the grains

Lots of white spots, compared to the 0 sccm and 7 sccm samples. These are much bigger than the grains, with typical lengths of from $0.2\mu m$ to between 0.75 and $1\mu m$ across.

20 sccm, 900°C: Most of the visible grains range in size from about $0.15\mu m$ to $0.9\mu m$ as measured across the widest part. However the white spots is as wide as $1.3\mu m$. The white spots seem to form lumps, having a rough structure. It is not visible whether these are clusters of individual grains or not. The pinholes also seem to have grown in size, so that the amount and size as compared to the grains is about the same as in the 800°C sample.

20 sccm, 1000°C: Typical grain size: $1 * 1\mu m^2$ or a little smaller. The white fields are clearly lumps, which seem to consist of smaller grains. These are a lot bigger than the other grains, about $1.7 * 2.5\mu m^2$. The large white clusters are partially surrounded by pinholes, separating each. The number of pin holes seems to be about the same as for the sample heated at 900°C: Lots of pinholes at sizes just a little bit smaller than these grains.

5.4 Errors and accuracy considerations

5.4.1 Hall measurement

Hall measurements were conducted in order to determine resistivity, ρ , carrier concentration, p , and mobility, μ , of the films, which were recorded at ten different field strengths. Ideally these ten measurements should give the same value for the different quantities. However, there was some variation, from which the number of valid digits could be determined. This has been taken into account in the errors as plotted in the results. For some measurements certain quantities varied a lot. In those cases the average value was used.

There also exists a geometrical error to the measured quantities. The Van der Pauw's analysis, upon which the measurement is based, assumes point-like contacts to the sample, which is not achievable in practice. For square samples the correction factors can roughly be expressed by the contact diameter, c , and side length of the sample, l , as:

$$\Delta\rho/\rho \propto (c/l)^2$$

$$\Delta p/p \propto c/l$$

$$\Delta\mu/\mu \propto c/l$$

When calculating the geometrical errors, a contacts size of 1.5 mm in diameter is assumed, while the sides of the samples are 10 mm. This gives a $\Delta\rho$ of 2.25%, while the Δp and $\Delta\mu$ is 15%.

5.4.2 Comparison of intensity of XRD peaks

In order to compare the intensity of XRD peaks for different N-flows and for different RTP temperatures, first the background was removed, and then the plots were normalized. The normalization was done after the intensity of the background peak in $2\theta = 64.5^\circ$ of the sample with highest value. For the heat treated samples the normalization was done separately for each N-flow.

5.4.3 FWHM and angle positions of XRD peaks

The FWHM and 2θ positions of the XRD peaks was estimated by the data program, EVA. Before the estimations the intensity from the $KK\alpha_2$ radiation was removed, so that no peaks appeared wider than it was. The estimation of FWHM and 2θ positions was done by choosing an appropriate area in the plot to include the peak of interest. Then EVA made an estimation of the peak properties. I made the program estimate the FWHM value and 2θ position five to six times for each peak, by varying the area of choice. In this an uncertainty of the estimated values was estimated and plotted as an error bar. In some of the plots, the error bar was smaller than the dots, and are not shown.

5.4.4 UV-vis measurements of heat treated samples

Many of the heat treated samples have small holes in the film. During the transmittance measurement I took out the sample holder in order to have better

control when placing the samples, so that the biggest holes could be avoided in the opening. However, for the 20 sccm sample heated at 900°C and 1000°C it was a small and a somewhat bigger hole, respectively, in the middle of the sample, which was not possible to avoid in the opening where the light beam is emitted.

5.4.5 Thickness measurement by SIMS

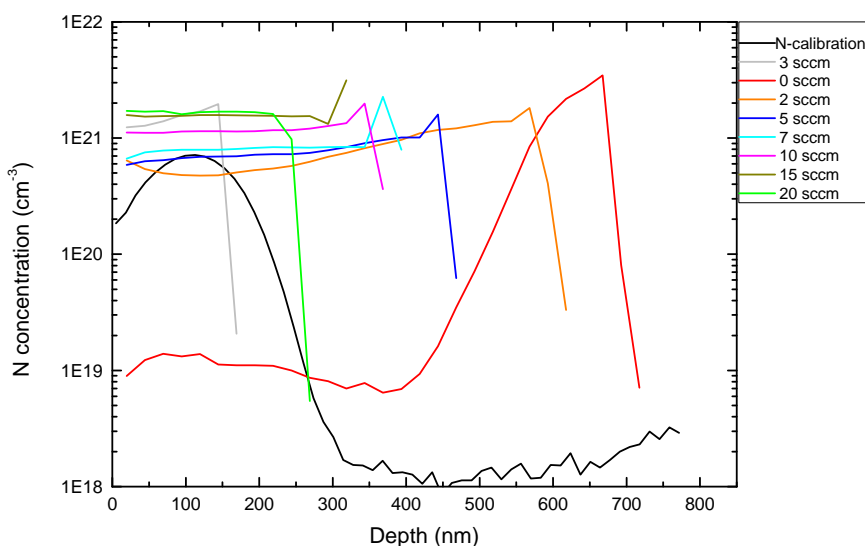


Figure 36: Profile of Cu by SIMS

The thicknesses of the deposited Cu_2O films were taken from the copper depth profiles as measured by secondary ion mass spectrometry (SIMS), shown in Figure 15. The thickness corresponds to the depth at which the signal stops. However, this depth is somewhat ambiguous, as seen from the profiles. First, the fall off is quite abrupt, but not totally. This means that the thickness will get 5 to 15 nm larger if measured at the lowest intensity, 1000 counts per second, than if measured at the point where the fall off begins. Secondly, for some of the films the intensity clearly falls in steps, which is the case for the films with an N flow of 0, 2, 3, 5 and presumably 7 sccm. This indicates that the stoichiometry in the interfacial region between the film and the quartz substrate is changed. The stoichiometry could contain less copper or it might be changed by something else that affects the electrical properties so that the ionization probability gets lower. This could also be due to roughness of the film at the interface between the film and the quartz substrate. The signal could also be lower in this region

because of variation in the energy of the primary ions. In these cases there is less straight forward to chose the measuring point. In addition to the points where the almost vertical fall off starts and stops, the thickness might be taken at the point where the intensity begin to fall just a little. It could also be taken somewhere in between these points.

As a choice I measured the thicknesses at the last kink points before the almost vertically decrease in intensity. Then I rounded this value to the closest five nanometers.

For the sample with N flow of 7 sccm the slope is not as steep as for the other films, and, unlike the other profiles, the signal is only recorded until it has decreased to about 15000 counts. Because of this I made an assumption that the last measurement point corresponded to the last kink before fall off. I did therefore not choose the kink at 375 nm as the thickness, but instead 400 nm, which corresponds to the last point of measurement.

The signal of the samples are compared with an N implanted Cu_2O reference sample. The corrosion rate is assumed to be constant, and the crater depth of the reference sample was measured afterwards. This is the basis for conversion of the recorded intensity versus time signal into intensity versus depth.

The depth resolution for this kind of SIMS measurement is generally 10 to 15 nm at it's best. In this measurement the resolution must have been lower than this. Variations in the energy of the primary ions and in the sputter rate affect the depth accuracy. Because of this the thicknesses as measured by SIMS might have an uncertainty of 5 to 10 %. However the choice of measuring point for the thickness has in some cases a larger insecurity. The sample for which the intensity falls off over the biggest depth interval is the 0 sccm film. It's intensity decrease first a little at 575 nm, while the last kink before fall off is at 675 nm, which is 100 nm deeper. This indicates that the accuracy of the thicknesses is within about 100 nm.

Accuracy considerations:

The read off value is accurate within 1 nm.

It could be speculated if there is more accurate to read the value off after the signal has decreased for a while. For instance the depth increase as the intensity drops off further. From the last kink to the point at which the intensity has dropped to 1000 counts the depth increase between 4 and 15 nm.

5.4.6 Grain sizes from SEM

The sizes of the grains as seen from the SEM pictures were measured by eye, using a ruler above the images.

6 Conclusion

The characterization results of the as-deposited films show that nitrogen doping of Cu_2O thin films by reactive magnetron sputtering gives higher carrier concentrations, resulting in lower resistivities of the films, which was the intention. The lowest resistivity value was achieved for the 20 sccm as-deposited film, having a value of $2.59\Omega\text{cm}$.

SIMS measurements have showed that the nitrogen concentration increases with N_2 -flow. Together with the result that carrier density increases with N_2 -flow, this is a clear indication that successful, substitutional doping of the Cu_2O films has been achieved.

XRD-measurements have confirmed that the as-deposited films have a pure Cu_2O phase, with no known contaminants.

Transmission measurements shows that the nitrogen doped films have a high absorption coefficient for wavelengths with energies higher than the band gap energy, and a large transmittance for lower energy wavelengths. The transmittance in the latter wavelength area varies around $\sim 60\%$.

The results of this thesis indicates that nitrogen doped cuprous oxide thin films are well suited for use in solar cells.

The films deposited with 0 sccm, 7 sccm and 20 sccm amount of N_2 -flow during deposition were subsequently heat treated at 800°C , 900°C and 1000°C for three minutes by RTP. However, this seems to have caused the nitrogen dopants to leave the samples. Hall measurements have shown that both carrier concentration and resistivity have decreased for the heat treated samples, as compared to the as-deposited samples of the same N_2 -flow. SEM images have shown that the grain size increases after heat treatment. Also, a large amount of holes occur in the films after heat treatment, especially for the films with nonzero N_2 -flow at 1000°C .

References

- [1] Ben G. Streetman & Sanjay Kumar Banerjee. *Solid State Electronic Devices*. Pearson, seventh edition, 2016.
- [2] Jr. William D. Callister and David G. Rethwisch. *Materials Science and Engineering: An Introduction*. John Wiley & Sons, Inc., eighth edition, 2009.
- [3] Yang Leng. *Materials Characterization: Introduction to Microscopic and Spectroscopic Methods*. Wiley-VCH Verlag GmbH & Co. KGaA, second edition, 2013.
- [4] Sandep M. Gorantla Edouard Monakhov Kristin Bergum, Heine N. Riise and Bengt G. Svensson. Thin film Cu_2O for solar cell applications. *IEEE Photovoltaic Specialists Conference*, 43, 2016. doi: 10.1109/PVSC.2016.7750156.
- [5] Charles Kittel. *Introduction to Solid State Physics*. John Wiley & Sons, Inc., seventh edition, 1996.
- [6] Stephen A. Campbell. *Fabrication Engineering at the Micro- and Nanoscale*. Oxford University Press, fourth edition, 2013.
- [7] D. Reppin M. Becker P. Hering P. J. Klar Th. Sander C. Reindl J. Benz M. Eickhoff C. Heiliger M. Heinemann J. Bläsing A. Krost S. Shokovets C. Müller B. K. Meyer, A. Polity and C. Ronning. Binary copper oxide semiconductors: From materials toward devices. *Physica Status Solidi (B)*, 249(8):1487–1509, 2012. doi: 10.1002/pssb.201248128.